

**DESIGNING AND SIMULATING WAVELENGTH SHIFTING
GEOMETRY IN AN ACTIVE HELIUM TARGET**

BY

ISABELLE F. DOLAN

A thesis submitted to the
Department of Physics
Mount Allison University
in partial fulfillment of the requirements for the
Bachelor of Science degree
with Honours
May, 2021

ABSTRACT

Scalar polarizabilities are fundamental characteristics closely related to the internal structure of nucleons. While the polarizabilities of the proton have been well studied, the neutron remains elusive due to the lack of a free-neutron target. Based at the Institute for Nuclear Physics in Germany, the A2 Collaboration has proposed a new active helium target filled with helium isotopes that would allow better access to the neutron. This design would allow for the collection of scintillation light within the active volume, which would reduce backgrounds. The blast of photons emitted from each collision are in the vacuum ultraviolet, while the silicon photomultipliers used only detect in the 200 – 900 nm range. Thus, a wavelength shifting material is needed. This research examines potential configurations of wavelength shifting fibers to be placed within the target and simulates the light collection and output of each design. Monte Carlo and Geant4 simulations were carried out to compare scintillation light collection between potential wavelength shifter geometries. The results of this work, along with future analysis, will provide integral insight for building the next prototype. Once the target is built, the neutron scalar polarizabilities can be applied to help explain quantum chromodynamics in the non-perturbative region.

ACKNOWLEDGMENTS

My greatest thanks goes to Dr. David Hornidge. Thank you for taking me on as a summer student and for teaching me most of what I know about experimental physics. Working under your supervision these past two years has been an absolute pleasure.

I would also like to thank Dr. Phil Martel from the A2 Collaboration, without whom this thesis would not have been possible. I am tremendously grateful for all of your help and guidance in every aspect of my honours work. Thank you for sharing your wealth of knowledge with me.

Moreover, thank you to my fellow research students from both summers, although I now consider you all dear friends. To Jenna and Mike, thank you for a great summer in Germany. From sleep deprived bus rides to watching a ridiculous amount of movies (see Die Hard), it was wonderful. Jenna, our (mis)adventures in Glasgow and Croatia are fond memories I'll never forget. To Selina, Alicia, and Heidi, although our summer was virtual, I am forever grateful to our Subatomic Physics group chat for providing me with laughs (and assignment help) all year long.

Finally, thank you to the people in my life outside of physics for your encouragement and support throughout my degree. To my parents and my grand-parents, thank you for always listening to me talk about physics, even if you didn't understand it. I can't express my gratitude for everything you have done for me.

Contents

| | |
|--|------------|
| ABSTRACT | i |
| ACKNOWLEDGMENTS | ii |
| TABLE OF CONTENTS | iii |
| LIST OF FIGURES | v |
| LIST OF TABLES | ix |
| GLOSSARY | xi |
| 1 INTRODUCTION | 1 |
| 1.1 The Standard Model | 1 |
| 1.2 Quantum Chromodynamics | 4 |
| 1.3 Nucleon Polarizabilities | 6 |
| 1.3.1 Electric Polarizability | 7 |
| 1.3.2 Magnetic Polarizability | 7 |
| 1.4 The Neutron Problem | 8 |
| 1.5 Active Helium Target Solution | 9 |
| 1.6 Coherent Compton Scattering | 10 |
| 2 EXPERIMENT | 12 |
| 2.1 Mainzer Mikrotron | 12 |
| 2.1.1 Electron Production | 12 |
| 2.1.2 Linear Accelerators | 13 |
| 2.1.3 Racetrack Microtrons | 14 |
| 2.1.4 Harmonic Double Sided Microtron | 16 |
| 2.2 A2 Hall | 17 |
| 2.2.1 Radiator | 17 |
| 2.2.2 Glasgow Tagged Photon Spectrometer | 19 |
| 2.2.3 Target | 21 |
| 2.2.4 Crystal Ball | 22 |

| | | |
|-------------------|---|-----------|
| 2.2.5 | Two Armed Photon Spectrometer | 23 |
| 2.3 | Monte Carlo Simulations | 25 |
| 2.3.1 | Event Generation | 26 |
| 2.3.2 | Standalone Monte Carlo Program | 26 |
| 2.3.3 | Geant4 | 27 |
| 3 | ACTIVE HELIUM TARGET | 28 |
| 3.1 | Active Component | 28 |
| 3.1.1 | Scintillation Yield | 30 |
| 3.2 | Design | 31 |
| 3.2.1 | Max-Lab Design | 32 |
| 3.2.2 | Glasgow Design | 33 |
| 3.2.3 | Silicon Photomultipliers | 35 |
| 3.3 | Prototype | 36 |
| 3.3.1 | SiPM Arrangement | 37 |
| 3.3.2 | Test Results | 39 |
| 3.4 | Investigating Wavelength Shifting | 40 |
| 3.4.1 | TPB | 40 |
| 3.5 | New WLS Designs | 41 |
| 3.5.1 | Acrylic Light Guides | 42 |
| 3.5.2 | Fiber Barrel Design | 43 |
| 3.5.3 | Fiber Helix Design | 45 |
| 4 | ANALYSIS OF NEW DESIGNS | 48 |
| 4.1 | Simulations | 48 |
| 4.1.1 | EvGen | 48 |
| 4.1.2 | Standalone Monte Carlo Code | 49 |
| 4.1.3 | A2Geant4 | 51 |
| 4.2 | Results | 53 |
| 4.2.1 | Acrylic Light Guides | 53 |
| 4.2.2 | Fiber Barrel | 54 |
| 4.2.3 | Fiber Helix | 59 |
| 5 | DISCUSSION AND OUTLOOK | 64 |
| REFERENCES | | 66 |

| | |
|--|-----------|
| A Tabulated Results | 69 |
| A.1 Calculation Method | 69 |
| A.2 Throwing Particles | 69 |
| A.3 Using EvGen Files as Input | 70 |
| B Possible Design Modifications | 72 |

List of Figures

| | | |
|-----|---|----|
| 1.1 | The current version of the Standard Model with the quarks in purple, the leptons in green, the bosons in red, and the Higgs boson in yellow [Wik20]. | 2 |
| 1.2 | Illustration of a proton without (left) and with (right) the presence of an electric field, \vec{E} [Hag16] | 7 |
| 1.3 | Illustration of a proton without (left) and with (right) the presence of a magnetic field, \vec{H} [Hag16]. Note the paramagnetic and diamagnetic components. | 8 |
| 1.4 | Schematic diagram of the Compton scattering process [Mor16]. A photon γ is incident upon a ^3He nucleus initially at rest. The photon is scattered away as γ' at an angle θ and the nucleus recoils following the straight arrow. | 11 |
| 2.1 | Floor plan at the MAMI facility, including the three RTMS, the HDSM, and the A2 Hall boxed in red [Kai08]. The other halls are shown here as well, which also utilize the electron beam for particle physics experiments. | 13 |
| 2.2 | Schematic diagram of first RTM at MAMI along with the energies from each step in the acceleration process [Col15]. The two large dipole magnets are shown in grey, the LINACs are shown in red, and the focusing devices are shown in blue along each track. | 14 |
| 2.3 | The three racetrack microtrons at MAMI along with the number of re-circulations done in each RTM. The schematic drawing highlights the “racetrack” nature of this accelerator system. | 16 |
| 2.4 | Schematic diagram of the HDSM at MAMI [Deh11]. The four bending magnets are shown in blue and the two LINACs are shown in red. . . . | 17 |
| 2.5 | A visual representation of bremsstrahlung. A negative electron decelerates when passing near a positive nucleus and emits the energy lost in the form of electromagnetic radiation [ICM21]. | 19 |

| | | |
|-----|--|----|
| 2.6 | The electron beam path through the radiator (shown as a brown rectangle on the left) to the Glasgow Tagged Photon Spectrometer. The photon beam path to the target along with the detector set-up around the target is also shown. | 21 |
| 2.7 | The Crystal Ball detector in the A2 Hall. The opening where some angular coverage is lost can be seen along with the PMTs and high voltage modules [MAM21]. | 23 |
| 2.8 | During an experiment, TAPS is placed close to the Crystal Ball to achieve necessary coverage; however this is a picture of the TAPS isolated. | 24 |
| 2.9 | Visualization of the CB-TAPS detector set-up in Mainz. The beam line enters the CB from the top right-hand side and passes through the target cell, shown here surrounded by the PID and tracking detectors in the center of the CB [Hor19]. | 25 |
| 3.1 | Ultraviolet emission spectrum of a high-pressure helium discharge lamp [Jeb13]. Helium scintillates primarily in the 70–95 nm range, with a peak at 80 nm. | 29 |
| 3.2 | Number of prompt UV photons produced by primary particle stopped in liquid helium. Dashed green line: helium atom recoil (alpha particle). Solid red line: electron [Ito13]. | 32 |
| 3.3 | Schematic drawing of the original MAX-Lab Helium Gas-Scintillator Active Target (HGSAT). | 33 |
| 3.4 | Sketch of Glasgow target, designed by D. J.R.M. Annand from the University of Glasgow. The main cylindrical cell is 40 cm in length and has a diameter of 102 mm, while the two extension tubes are 40 cm each [Ann14]. | 34 |
| 3.5 | Detection efficiency of the Sens-L silicon photomultipliers to be employed in the AHeT [Sen17]. One can see that they are most efficient in the 200–900 nm range, with a PDE at 420 nm. | 36 |
| 3.6 | The prototype AHeT used for testing [Per17]. This was only 40 cm in length compared to the Glasgow design’s 80 cm and suffered from reduced coverage. | 37 |

| | | |
|------|---|----|
| 3.7 | Pictured are SiPM diodes running down each of the eight PCBs. The channels follow the same colour scheme as seen Figure 3.8, with the first three SiPM diodes of each PCB are in channel 1, the next three are in channel 2, etc. [Per17]. | 38 |
| 3.8 | Pictured is the PCB arrangement within the prototype target, with each coloured ring representing a channel [Per17]. | 39 |
| 3.9 | Re-emission spectra of a $1.8 \mu\text{m}$ TPB film for several incident wavelengths. No dependence on incident wavelength was observed [Ben18]. | 41 |
| 3.10 | Pictured is a sample of the acrylic light guide design one PCB shown in green, the SiPM diodes shown in black, and the acrylic light guides on top of each SiPM shown in white. One TPB coating is drawn on the first light guide in blue. | 42 |
| 3.11 | Acrylic light guide configuration in the target shell. For illustrative purposes, only one array of acrylic light guides is coated in TPB (blue), although all would be coated in practice. This drawing is not to scale. | 43 |
| 3.12 | The barrel design in the target shell with one ring of SiPMs shown at the top. The TPB doped fibers, in green, are also shown. It is important to note that this is not exactly to scale, contrary to the Geant4 drawings. | 44 |
| 3.13 | Geant4 rendering of the barrel design, with the fibers in blue and the scintillation photon trajectories in green. The scintillation light shown in this figure is the result of a 1 MeV alpha particle being thrown in the barrel design. | 45 |
| 3.14 | A sample of one helix with the photon beam axis following the blue arrow. | 46 |
| 3.15 | A drawing of the helix design from Geant4. This shows the ring design, used to approximate the results that would be obtained by the helix design. The bright line along the cylinder axis represents the SiPMs. The scintillation light shown in green is the result of a 1 MeV alpha particle being thrown in the target. | 47 |
| 4.1 | The initial position of each event as defined by the standalone MC program, shown as black dots. This is an example of 2000 events distributed isotropically in the target volume. | 50 |

| | | |
|------|--|----|
| 4.2 | The blast of photons produced by each event, with each photon having a specified trajectory. This is an example of 2000 events distributed isotropically in the target volume. | 51 |
| 4.3 | Energy deposited in the SiPMs per event (left) and the hits per SiPM per event (right). | 52 |
| 4.4 | Photon output for the acrylic light guide design. Here, a photon is successful if it hits the sample of geometry. | 54 |
| 4.5 | Photon output per event for the fiber barrel design. | 55 |
| 4.6 | Hits per SiPM for various particle types at 5 (black), 10 (blue), and 15 (red) MeV. The scintillation yield was held constant at 65. | 56 |
| 4.7 | Hits per SiPM for α particles (black), protons (magenta), and photon (green). The scintillation yield was set to 65, 650, and 6500. | 57 |
| 4.8 | Hits per SiPM for Compton scattering off ${}^3\text{He}$ at 100, 150, and 200 MeV and neutral pion production at 150 and 200 Mev, with a scintillation yield of 65. | 58 |
| 4.9 | Hits per SiPM for Compton scattering and neutral pion production at 200 MeV. The simulation was run with a scintillation yield of 65 (black), 650 (magenta), and 6500 (green). | 58 |
| 4.10 | Photon output per event for the fiber helix design. | 60 |
| 4.11 | The leftmost histogram shows the hits per SiPM for α particles being thrown in the helix design with a set scintillation yield of 65. The histogram on the right shows the hits per SiPM for a 5 MeV α particle at the three scintillation yields. | 61 |
| 4.12 | Hits per SiPM for Compton scattering off ${}^3\text{He}$ at 100, 150, and 200 MeV and neutral pion production at 150 and 200 Mev, with a scintillation yield of 65. | 62 |
| 4.13 | Hits per SiPM for Compton scattering and neutral pion production at 200 MeV. The simulation was run with a scintillation yield of 65 (black), 650 (magenta), and 6500 (green). | 62 |

List of Tables

| | | |
|-----|--|----|
| 1.1 | The four forces and their respective strength, theory, and mediator. The cited relative strengths are estimates and actual values vary [Gri10]. | 4 |
| 1.2 | The current accepted scalar polarizabilities for the proton and neutron along with their corresponding uncertainty [Pat16]. The error associated with the neutron's measurements are approximately three times as large as the proton's. | 9 |
| 4.1 | Summary of the main processes and energies considered with EvGen. | 49 |
| 4.2 | Hits per SiPM results for Compton scattering on ^3He and neutral pion production in the barrel design at various photon beam energies and scintillation yields. | 59 |
| 4.3 | Hits per SiPM results for Compton scattering on ^3He and neutral pion production in the helix design at various photon beam energies and scintillation yields. | 63 |
| A.1 | Mean hits per SiPM results for different particles thrown in the barrel design at 5, 10, and 15 MeV and for scintillation yields set at 65, 650 and 6500 photons emitted per MeV of energy deposited in the active volume. | 69 |
| A.2 | Mean hits per SiPM results for different particles thrown in the helix design at 5, 10, and 15 MeV and for scintillation yields set at 65, 650 and 6500 photons emitted per MeV of energy deposited in the active volume. | 70 |
| A.3 | Hits per SiPM results for Compton scattering on ^3He and neutral pion production in the barrel design at various photon beam energies and scintillation yields. | 71 |
| A.4 | Hits per SiPM results for Compton scattering on ^3He and neutral pion production in the helix design at various photon beam energies and scintillation yields. | 71 |
| B.1 | Possible fiber to SiPM couplings for the barrel and ring designs. | 72 |

GLOSSARY

| | |
|-----------|---|
| ADC | Analogue-to-Digital Converter |
| AHeT | Active Helium Target |
| CB | Crystal Ball |
| χ PT | Chiral Perturbation Theory |
| CW | Continuous Wave |
| DC | Direct Current |
| EM | Electromagnetic |
| EvGen | Event Generator |
| HDSM | Harmonic Double Sided Microtron |
| LINAC | LINear ACcelerator |
| MAMI | MAinz MIcrotron |
| MC | Monte Carlo |
| Non-pQCD | Non-Perturbative Quantum Chromodynamics |
| PID | Particle Identification Detector |
| PCB | Printed Circuit Board |
| PMT | PhotoMultiplier Tube or also Phototube |
| QCD | Quantum ChromoDynamics |
| QED | Quantum ElectroDynamics |
| RTM | RaceTrack Microtron |
| SiPM | Silicon PhotoMultiplier |
| S/N | Signal-to-Noise |
| SM | Standard Model |
| TAPS | Two Armed Photon Spectrometer |
| TDC | Time-to-Digital Converter |
| TPB | TetraPhenyl Butadiene |
| VUV | Vacuum Ultra-Violet |

Chapter 1

INTRODUCTION

1.1 The Standard Model

If an everyday object were continually cut into smaller and smaller pieces, where would one end up? Could this go on forever, or would there eventually be a point where the matter has reached its smallest representative element? When the Greek philosopher Democritus posed this question in 430 BCE, he rationed the existence of a set of uncuttable building blocks. He called these “atomos,” meaning indivisible [Led93]. Although the atom does in fact divide into smaller constituents (the proton and the neutron), the question “What is matter made of” is at the heart of subatomic particle physics. From the 1940s through the 1960s, hundreds of subatomic particles were discovered. In order to determine what held nuclei together, many accelerator experiments were made in which particles with higher and higher energies were collided together. When the energies became sufficiently high, these collisions resulted in not only protons and neutrons, but also in large, new particles [Fey14]. These unexpected results posed the question: were there an infinite number of particles in the world? Eventually, it was discovered that protons and neutrons were made up of even smaller particles, called quarks. The findings from these collision experiments along with our current understanding of the building blocks of the universe can be summarized by the Standard Model (SM). The SM can be divided into two parts: the “matter” particles, such as quarks, electrons, muons, etc., and “interactions,” such as the weak force, the strong force, etc. The matter particles are spin-half particles and obey the Pauli exclusion principle, which prevents more than

one particle from being in the same state. This explains why we can have solid objects that do not collapse to a point or radiate away to infinity [Haw94]. The three leftmost columns of Figure 1.1 are comprised of these spin-half particles, called fermions. The last two columns represent the integer-spin particles, called bosons, that do not obey the Pauli exclusion principle. Figure 1.1 shows the SM further subdivided into its four categories: quarks, leptons, gauge bosons, and the Higgs boson. This theoretical framework explains the interactions between quarks and leptons and their respective force carriers (bosons). Each of these particle also has an anti-particle counterpart, not shown in Figure 1.1.

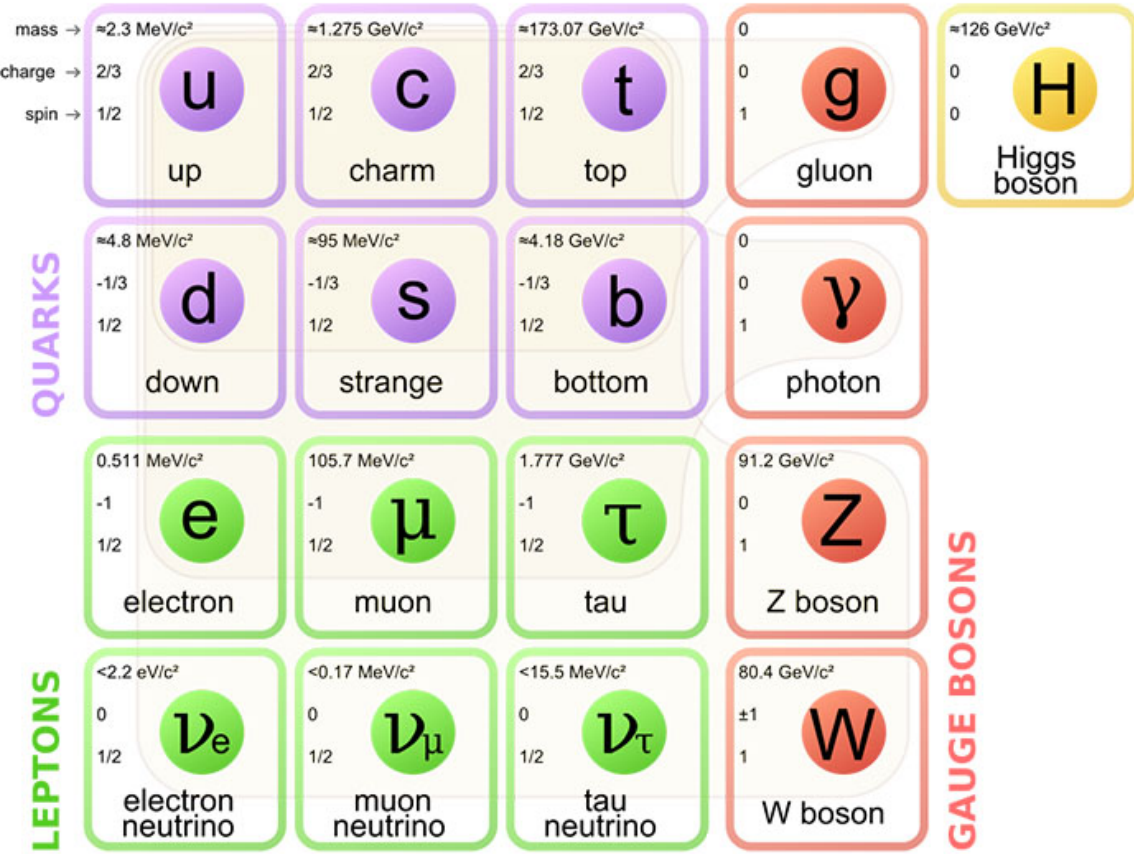


Figure 1.1: The current version of the Standard Model with the quarks in purple, the leptons in green, the bosons in red, and the Higgs boson in yellow [Wik20].

The quarks, shown in purple, come in six flavours: up (u), down (d), charm (c), strange (s), top (t), and bottom (b). Quarks form the family of hadrons, which consists of baryons and mesons. Baryons are groups of three quarks, whereas mesons are quark/anti-quark pairs. The proton is a baryon made up of two u 's and one d quark, while the neutron is made up of two d 's and one u quark. The other quarks are necessary for explaining the vast number of discoveries made in particle accelerators. Quarks and their mediator particle, gluons, will be discussed in greater detail in later sections.

The green section of the SM accounts for the leptons. The most popular of this class is the electron (e), although there exist five other leptons: muon (μ), tau (τ), electron neutrino (ν_e), muon neutrino (ν_μ), and tau neutrino (ν_τ). The top three leptons have electrical charge of -1, while the bottom three neutrinos are neutral. These fermions have no internal structure and can be seen as point particles. Therefore, although the the τ is 3477 times more massive than the e , size is a meaningless characteristic when describing them.

Our present understanding of the universe gives rise to four fundamental forces: strong, electromagnetic, weak, and gravitational. Each of these forces has a relative strength and corresponding theory, as shown in the Table 1.1. They also have respective mediator particles, called gauge bosons, shown in red in Figure 1.1. These messenger particles transmit information between particle X and particle Y and allow them to interact with each other. Otherwise, particle Y would not know particle X is exerting a force on it. Each boson has a specific mass, charge, and spin-1. The gluon, which transmits the strong force, is a massless particle. The zero mass indicates that the strong force has a very far reach. However, it is so strong that quarks cannot get very far from one another [Led93]. Directly below the gluon in the SM is the photon. This well known particle carries the electromagnetic force and like the gluon,

it reaches out to infinity due to its zero mass. The W^\pm and Z bosons mediate the weak force and because of their large mass, only act over small distances. There is also a particle for gravity, called graviton, which has yet to be proven. Each of the fundamental forces can be successfully described by the SM save gravity. The latter is best described macroscopically by Einstein's general theory of relativity [Kie13]. A quantum formulation of gravity that can be included in the framework of subatomic particle physics is one of the central questions of 21st century physics.

| Force | Strength | Theory | Mediator |
|-----------------|------------|------------------|-------------------------|
| Strong | 10 | Chromodynamics | Gluon |
| Electromagnetic | 10^{-2} | Electrodynamics | Photon |
| Weak | 10^{-11} | Flavordynamics | W and Z |
| Gravitational | 10^{-42} | Geometrodynamics | Graviton (hypothetical) |

Table 1.1: The four forces and their respective strength, theory, and mediator. The cited relative strengths are estimates and actual values vary [Gri10].

Experimentally confirmed in 2012, the most recent addition to the SM is the quantum of the Higgs field, called the Higgs boson [Aad12]. This new field imparts mass to quarks, leptons, and W^\pm and Z bosons [Neg21].

1.2 Quantum Chromodynamics

Quantum electrodynamics (QED) has been used to successfully describe electromagnetism for decades. It claims that electrically charged particles act on one another through the quanta of the field, in this case photons. Physicists searched for a similar theory for the strong force, which resulted in quantum chromodynamics (QCD). This quantum field theory pertains to quarks and gluons and acts on anything with

“colour”. Colour is an additional characteristic associated with these two types of particles, although the word is not used in the traditional sense [Fey14]. A quark can be in one of the one of six conditions: red, green, or blue along with the corresponding “anti” state of each colour. The SM states that any combination must result in white; red, green, and blue is colourless and so is red plus anti-red. This can be used to explain why quarks can never exist isolated and come exclusively in groups on three (baryons) or quark plus anti-quark pairs (mesons).

QCD has two predominant features: asymptotic freedom and confinement [Col15]. As the distance between two quarks decreases, asymptotic freedom requires that the strong force decreases as well until the quarks act as free particles. Small distances imply high externally applied energy, thus, asymptotic freedom can also be viewed as the strong force getting weaker at high energies. When quarks get close together such that they act as essentially free, non-interacting particles, the coupling constant, α_s , is small and perturbative QCD (pQCD) may be used [Hal84]. As two quarks separate in distance, confinement demands that the force between them increases due to α_s also growing. Eventually, before the two particles separate, it becomes more energetically favourable to produce a new quark/anti-quark pair than to have two isolated quarks. QCD is therefore governed by confinement at lower energies. With α_s being sufficiently large, the higher terms in the Taylor expansion may no longer be ignored and non-perturbative QCD (non-pQCD) theories must be used. As QCD in the non-perturbative regime is not well understood, it is important to gain a better foothold. The theories that describe the confinement region are tested by comparing theoretical prediction with experimental results. One such method of verification is by measuring the scalar polarizabilities of a nucleon using Compton scattering.

1.3 Nucleon Polarizabilities

Like mass or charge, polarizabilities are fundamental structure constants. They indicate the degree to which the internal structure of a nucleon responds to an externally applied electromagnetic field. They therefore provide important information on the force holding the nucleus together. Polarizabilities come in two types: scalar and spin. The scalar polarizabilities are obtained from the second order expansion of the Hamiltonian in incident photon energy whereas the spin polarizabilities are obtained from the third order expansion. This thesis will focus on the two scalar polarizabilities: the electric and the magnetic. These two values are called α_{E1} and β_{M1} , respectively, and are shown in the second order expansion of the Hamiltonian in Eq. 1.1 along with the electric field E and magnetic field H [Hor15].

$$H_{eff}^{(2)} = -4\pi \left[\frac{1}{2}\alpha_{E1}\vec{E}^2 + \frac{1}{2}\beta_{M1}\vec{H}^2 \right] \quad (1.1)$$

Testing QCD models in the non-pQCD regime is accomplished by precise measurements of these polarizabilities. They are experimentally accessible through the analysis of the observables from Compton scattering experiments [Ann15]. The electromagnetic field of the scattered photon is used to probe the nucleon's response to an applied electric or magnetic field (see Section 1.6). The experimentally determined values can then be compared to the theoretically calculated ones. Seeing as different models give different results, the theoretical models that do not agree with the experiment may be refined or disregarded [Hor20].

1.3.1 Electric Polarizability

When an atom is placed in a homogeneous electric field \vec{E} , the positive and negative charges separate resulting in an induced electric dipole moment, $\vec{p} = \alpha_{E1}\vec{E}$, where α_{E1} is the proportionality coefficient, also known as the electric dipole polarizability [Shu09]. In a nucleon, a similar process takes place except the electrons and nucleus are replaced by the “pion cloud” and a quark core [Hag16]. When placed in an electric field, charge separation occurs among the virtual charged pions which stretches the nucleon in the direction of the field, as seen in Figure 1.2. The term “stretchability” was coined for the electric dipole polarizability due to the resulting deformation.

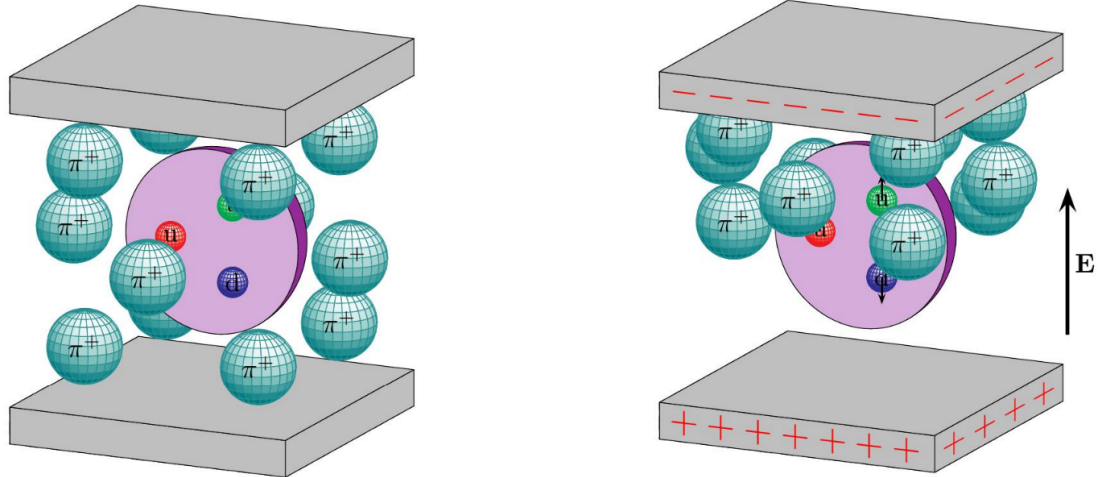


Figure 1.2: Illustration of a proton without (left) and with (right) the presence of an electric field, \vec{E} [Hag16]

1.3.2 Magnetic Polarizability

Analogously, the magnetic dipole moment is induced in the presence of an applied magnetic field, \vec{H} , and is given by $\vec{m} = \beta_{M1}\vec{H}$. The proportionality coefficient is the magnetic dipole polarizability, called β_{M1} . This value is also known as “alignability”

due to the fact that it describes the degree to which the dipoles of the internal constituents of the nucleon will align with the applied magnetic field. The total value of β_{M1} is given by $\beta_{M1} = \beta_{para} + \beta_{dia}$, where *dia* and *para* stand for the diamagnetic and paramagnetic components, respectively. The diamagnetic contribution of the pion cloud competes against the more dominant paramagnetic contribution of the quark-core thus partially canceling out their effects (see Figure 1.3). This results in β_{M1} being smaller than α_{E1} , as seen in Table 1.2.

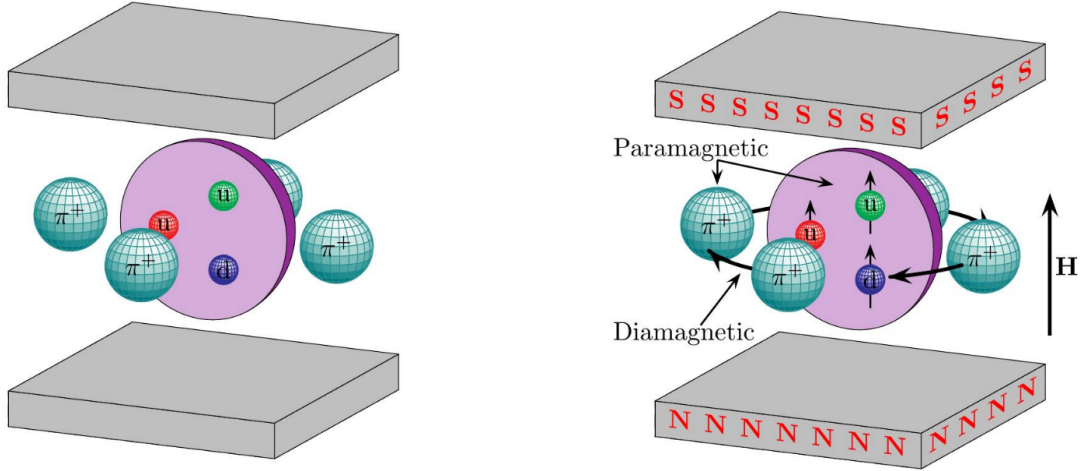


Figure 1.3: Illustration of a proton without (left) and with (right) the presence of a magnetic field, \vec{H} [Hag16]. Note the paramagnetic and diamagnetic components.

1.4 The Neutron Problem

Many research teams are dedicated to extracting these aforementioned scalar polarizabilities with lower uncertainty. One such research group is the A2 collaboration at the Mainz Microtron, who have undertaken a multi-experiment project to extract these polarizabilities [KPH19]. Previous work includes, but is not limited to, Compton scattering off deuterium, liquid ${}^4\text{He}$, carbon, oxygen, and liquid hydrogen [Tho16].

Table 1.2 outlines the current accepted values for the neutron and proton scalar polarizabilities.

| Nucleon | α_{E1} ($\times 10^{-4}$ fm 3) | β_{M1} ($\times 10^{-4}$ fm 3) |
|---------|--|---|
| Proton | 11.2 ± 0.4 | 2.5 ± 0.4 |
| Neutron | 11.8 ± 1.1 | 3.7 ± 1.2 |

Table 1.2: The current accepted scalar polarizabilities for the proton and neutron along with their corresponding uncertainty [Pat16]. The error associated with the neutron's measurements are approximately three times as large as the proton's.

It can be observed that the measurements for the proton are quite successful, while there are larger errors associated with the neutron. In fact, through various experiments on the proton, its electric and magnetic polarizabilities have been effectively pinned down [Shu09]. If one desires to study its internal structure, it suffices to use a target of liquid hydrogen and place it in the beam-line. Then, all of the Compton events detected would be due to photons scattering off of the proton directly. However, an analogous free-neutron target is not feasible. This is ascribable to the fact that the neutron has a short half-life of only 15 minutes. An isolated target would decay too quickly and is thus impractical. Previous work carried out using more complex and stable nuclei, including neutron scattering from the Coulomb field of ^{208}Pb and Compton scattering on the deuteron, yielded unsatisfactory results [Ann13].

1.5 Active Helium Target Solution

A paper published in 2009 [Shu09] shows that ^3He Compton scattering is an exciting prospect for mining the neutron scalar polarizabilities. The Compton cross section of ^3He is more sensitive to the neutron electromagnetic dipole polarizabilities than that of the deuteron [Shu09]. Furthermore, the probability that a Compton event will occur increases due to the presence of the extra proton in the nucleus, allowing

for more data to be collected compared to a deuterium target. The extraction of the polarizabilities will depend on Chiral Perturbation Theory (χ PT) [Ann13].

Proposed by the A2 Collaboration, the Active Helium Target (AHeT) is the name for the cell containing the gaseous ^3He that will be used at the Mainz Microtron. Nobles gases, such as He, have the convenient property of being excellent scintillators. That is, when struck with an energetic particle, they emit a flash light [Jeb13]. In this experiment, the He plays the role of target *and* scintillator. When struck by a photon during a Compton event, the He nucleus emits scintillation light in the vacuum ultra violet (VUV). While still in the prototype stage, this project is due to be completed within the next 4 years. Once complete, it will allow better extraction of the neutron scalar polarizabilities from Compton scattering data.

1.6 Coherent Compton Scattering

When a photon scatters off of the nucleus as a whole rather than quasi-freely off one one of the protons or the neutron, it is referred to as coherent Compton scattering. For the proposed ^3He experiment, the reaction goes as follows:



When a photon is incident upon a stationary nucleus, an exchange of energy occurs and the photon is scattered away at a smaller energy while the nucleus, having gained energy, is scattered simultaneously. This is schematically depicted in 1.4. As mentioned in Section 1.3, coherent Compton scattering is the method through which the polarizabilities are obtained. The outgoing scattered photon plays the role of the applied electromagnetic field and knowledge of its angle and energy can be used to retrieve all remaining properties, such as the scalar polarizabilities.

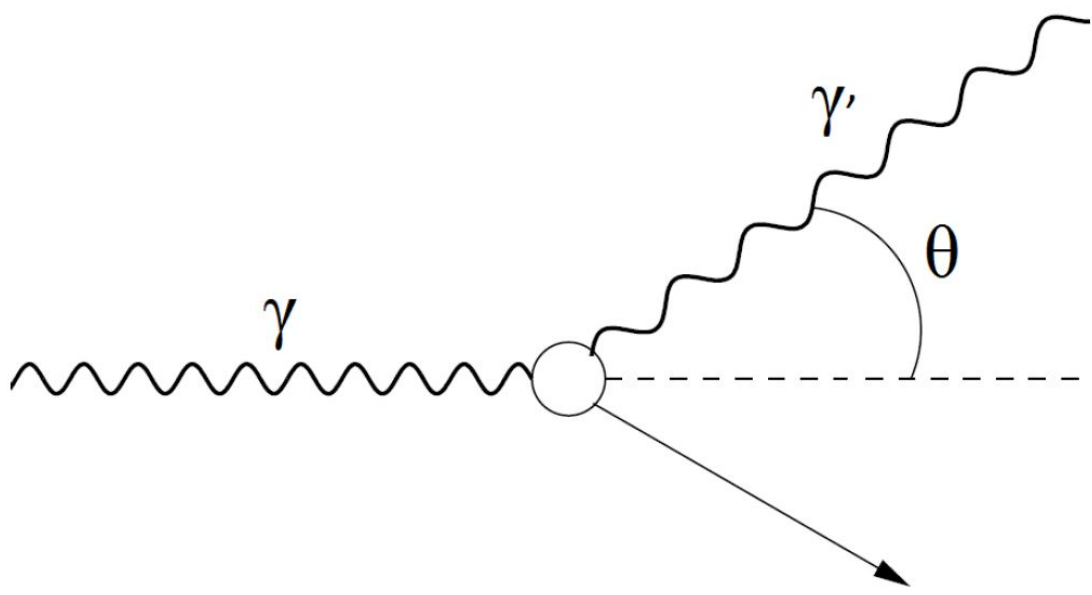


Figure 1.4: Schematic diagram of the Compton scattering process [Mor16]. A photon γ is incident upon a ${}^3\text{He}$ nucleus initially at rest. The photon is scattered away as γ' at an angle θ and the nucleus recoils following the straight arrow.

Chapter 2

EXPERIMENT

The Mainzer Mikrotron (MAMI) is a microtron shared by several research groups at the Institut für Kernphysik at the Johannes Gutenberg Universität in Mainz, Germany. The continuous wave of highly energetic electrons produced by MAMI is used by the A2 Collaboration to produce the photon beam needed for hadron experiments, namely the anticipated AHeT experiment. While electron production and acceleration are done by MAMI, photon production and detection are completed within the A2 Hall, boxed in red in Figure 2.1. The following chapter outlines both electron production and the journey of the photon beam from radiation to Compton scattering and detection.

2.1 Mainzer Mikrotron

First operational in 1979, MAMI is a continuous wave (100% duty factor) accelerator for electron beams used in high energy and nuclear physics [KPH09]. The acceleration of electrons happens in three distinct steps: (1) electron injector linear accelerator (LINAC) (2) a cascade of three racetrack microtrons (RTMs) and (3) the double-sided harmonic microtron.

2.1.1 Electron Production

Depending on the requirements of the experiment being run at the time, MAMI may produce electrons in one of two ways. For an unpolarized beam, 100 keV electrons are boiled off a DC electron gun via thermionic emission [Col15]. For a polarized

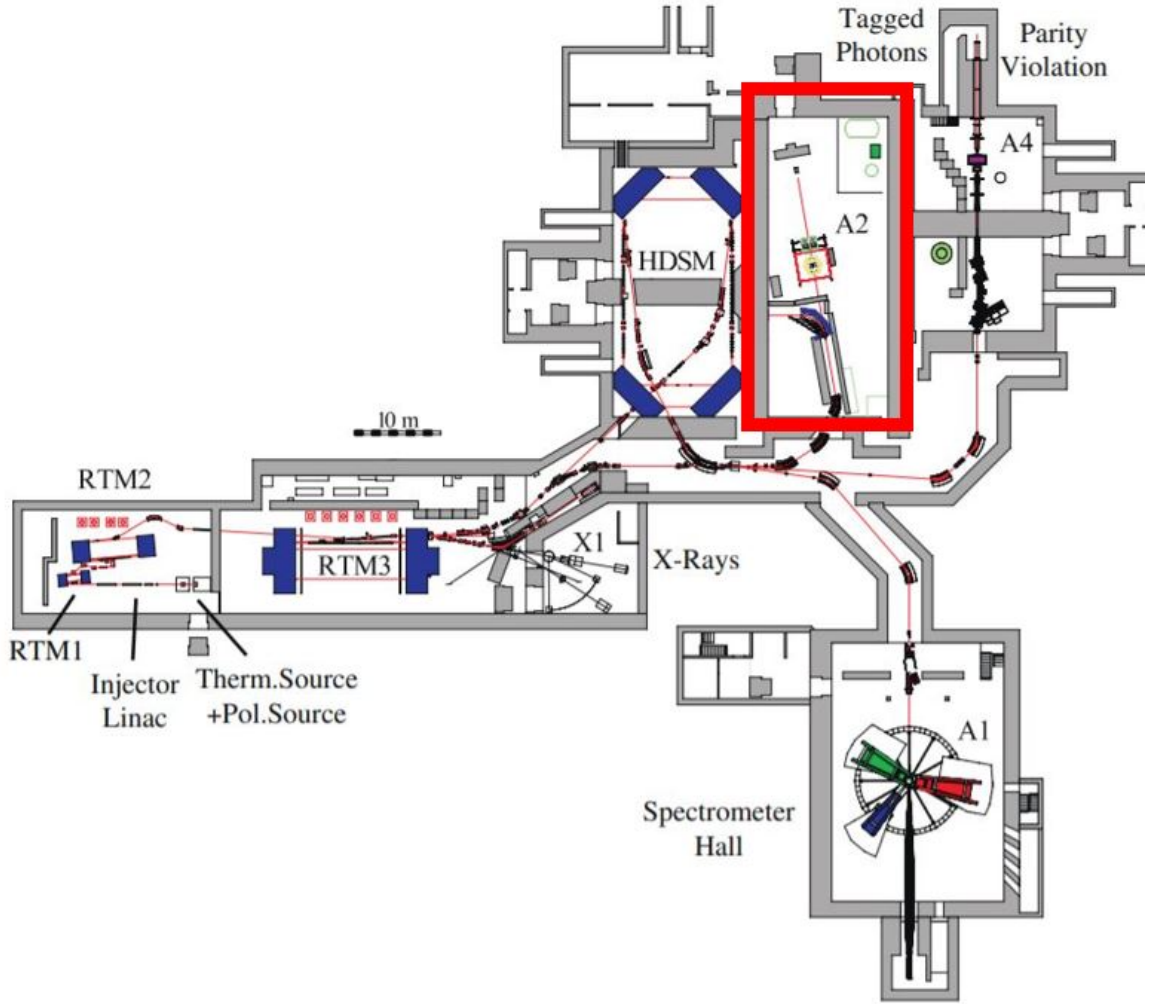


Figure 2.1: Floor plan at the MAMI facility, including the three RTMS, the HDSM, and the A2 Hall boxed in red [Kai08]. The other halls are shown here as well, which also utilize the electron beam for particle physics experiments.

beam, a laser-driven source creates electrons with 80% spin polarization [Wik21]. The electrons are then fed into a linear accelerator for an initial boost in energy. The active Helium target would use a non polarized electron source.

2.1.2 Linear Accelerators

Linear accelerators, or LINACs, are used in each step of the acceleration process. After the electron beam is produced, it is given its first boost in energy by the injector

LINAC, and exits with a total energy of 4.1 MeV. LINACs are comprised of several LC circuits which in turn use inductors (L) and capacitors (C) to attract and repel electrons [Hoo17]. The circuit is carefully tuned such that its oscillation successfully accelerated the electrons to the desired energy.

2.1.3 Racetrack Microtrons

To obtain the desired beam energy produced at MAMI, the electrons must pass through a LINAC multiple times. It would be unrealistic to assemble numerous LINACs in a series, and so a cascade of racetrack microtrons (RTMs) is employed instead. Each RTM is composed of a LINAC sandwiched between two large bending dipole magnets, as seen in Figure 2.2.

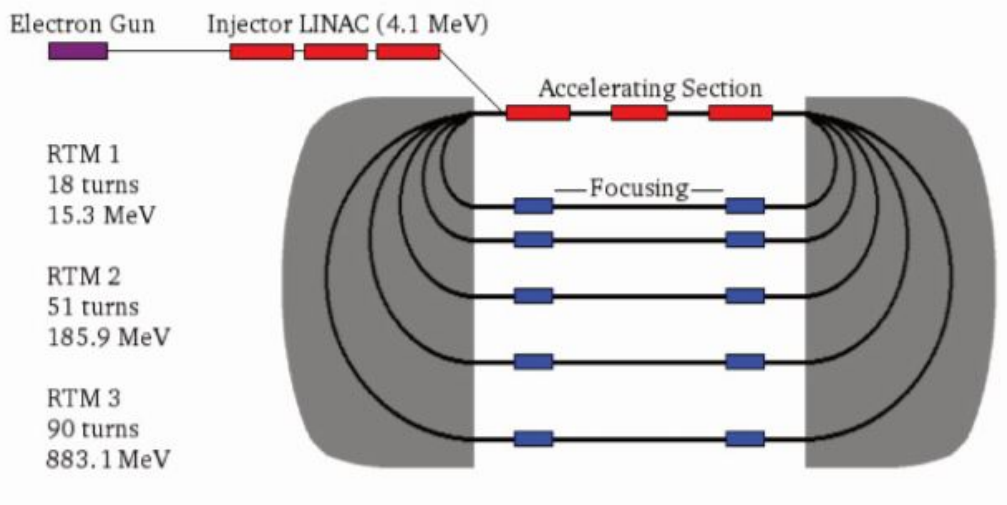


Figure 2.2: Schematic diagram of first RTM at MAMI along with the energies from each step in the acceleration process [Col15]. The two large dipole magnets are shown in grey, the LINACs are shown in red, and the focusing devices are shown in blue along each track.

After an electron passes through the LINAC, its trajectory is bent 180° by the first dipole magnet, then passed through a focusing device, then bent 180° by the second

magnet. This allows the electrons to be passed through the same LINAC multiple times and circumvents the kilometers of accelerators that would be needed otherwise. This beam re-circulation is also where the term “racetrack” comes from. Due to the electron’s increasing momentum, each path has a larger radius of curvature than the last. The path length gained in each successive lap, Δs , can be expressed by

$$\Delta s = 2\pi \frac{\Delta T_{RTM}}{e\beta c B}, \quad (2.1)$$

where ΔT is the increase in energy per turn and B is the strength of the the dipole magnet field. At MAMI, the electrons travel close to the speed of light and so $\beta \approx 1$. Once the electron is too energetic to be contained by the first RTM, it is passed to RTM 2, then RTM 3, with each microtron having larger magnets than the last. By the final RTM, the weight of the dipole magnets is over 900 metric tons combined and the beam is ejected with an energy of 883.1 MeV [Col15]. Further electron acceleration using this method would require dipole magnets of impractical sizes, and so the Harmonic Double Sided Microtron is employed instead.

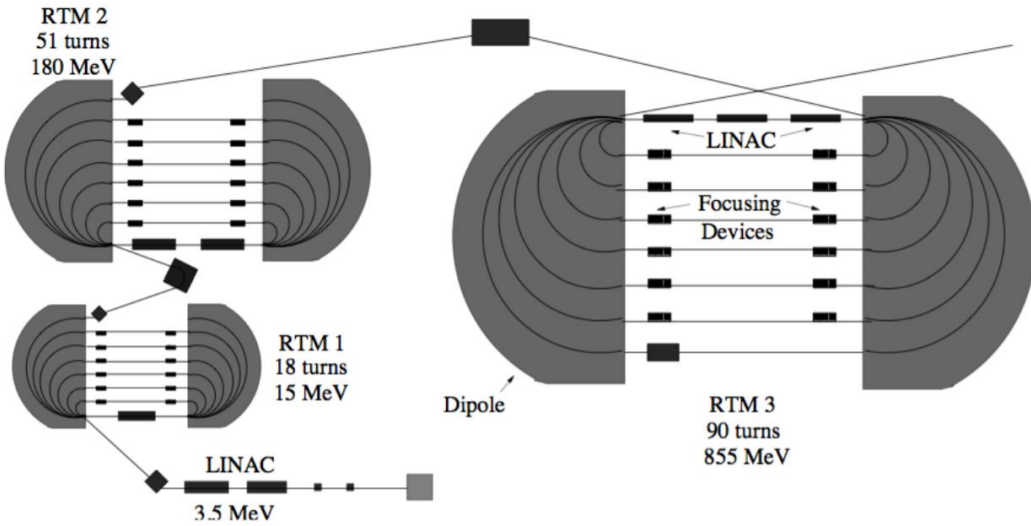


Figure 2.3: The three racetrack microtrons at MAMI along with the number of recirculations done in each RTM. The schematic drawing highlights the “racetrack” nature of this accelerator system.

2.1.4 Harmonic Double Sided Microtron

For experiments requiring electron beam energies exceeding 883.1 MeV, the beam is passed through the Harmonic Double Sided Microtron, or HDSM. Depicted schematically in Figure 2.4, although the HDSM has the advantage of lighter bending magnets, it is also more complicated than an RTM [Her76]. After entering the HDSM, the electrons are bent by 90° by each of the first two magnets, accelerated by LINAC I, bent by 90° at the second and third magnets, and passed through LINAC II. This process occurs up to 43 times to reach a final energy of up to 1.5 GeV. The components of the magnets weigh up to 130 tons, which is significantly less than the weight of equivalent dipole magnets that would be needed in a racetrack microtron to achieve 1.5 GeV in output beam energy [Kai08].

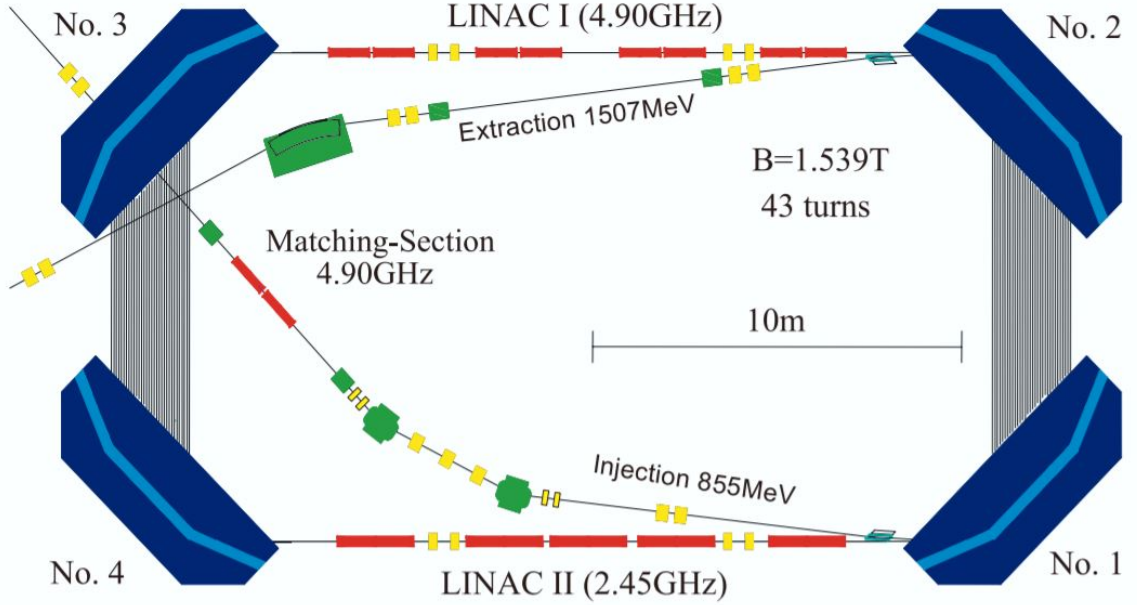


Figure 2.4: Schematic diagram of the HDSM at MAMI [Deh11]. The four bending magnets are shown in blue and the two LINACs are shown in red.

2.2 A2 Hall

Once the desired electron energy is achieved, the beam may then be directed into the A2 Hall using a series of focusing and bending magnets. The scattering experiments conducted by the A2 Collaboration do not directly use the electron beam in collision experiments. Instead, the beam is passed through a radiator which produces photons via the bremsstrahlung process. These photons are then directed to the target where the photo-nuclear reactions take place.

2.2.1 Radiator

As mentioned in Section 2.2, once in the A2 hall, a radiator is used to create a photon beam via bremsstrahlung. Meaning “braking radiation” in German, bremsstrahlung is the process where electromagnetic radiation is emitted by a charged particle when it

is deflected by another charge particle, as seen in Figure 2.5. More specifically, when the electron beam passes through the radiator material, the electrons interact via the Coulomb force with the positively charged nuclei contained in it. An electron will decelerate when passing near a positive nucleus and lose some of its kinetic energy. However, conservation of energy must stand and so the lost energy is emitted in the form of a photon, with the conservation requirements outline in the equation below:

$$E_\gamma = E_e - E_{e'}. \quad (2.2)$$

Here, E_γ is the emitted photon energy, E_e is the electron energy before radiating, and $E_{e'}$ is the electron energy post-bremsstrahlung. The astute reader may notice that the recoil nucleus energy, E_N , is not included in Eq. 2.2. This is due to the fact that E_N is proportional to the square of its momentum and its contribution in Eq. 2.2 is negligible [Wen17]. The atomic structure of radiator material used decides the degree of polarization of the photon beam produced. For a photon beam with no distinct polarization, a radiator material with an amorphous atomic structure may be used, such as a thin copper foil. For a polarized photon beam, a radiator with a lattice atomic structure is need, such as a diamond radiator.

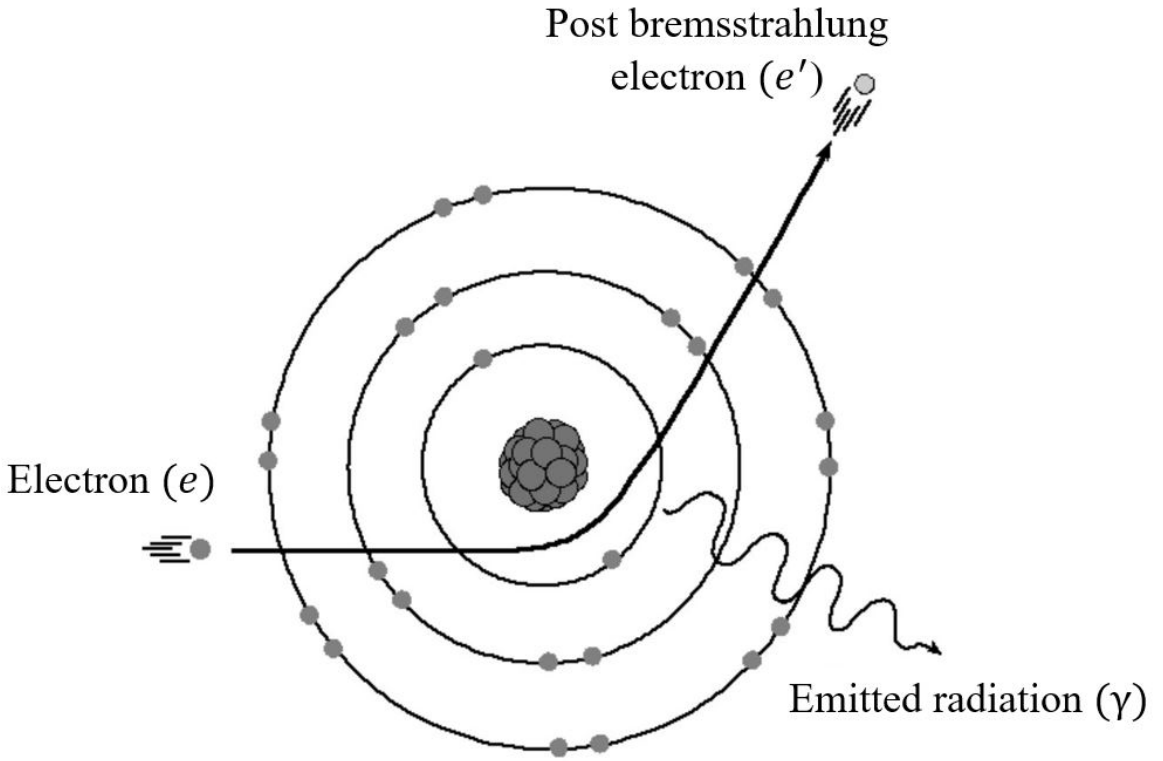


Figure 2.5: A visual representation of bremsstrahlung. A negative electron decelerates when passing near a positive nucleus and emits the energy lost in the form of electromagnetic radiation [ICM21].

2.2.2 Glasgow Tagged Photon Spectrometer

In scattering experiments with a stationary target, the incident particle's energy is a vital measurement. The Glasgow Tagged Photon Spectrometer, or simply the tagger, as been used in the A2 Hall to accurately extract the energy of incident photons since 1991 [McG08]. Seeing as the initial electron's energy, E_e , is known, the photon's energy, E_γ , can be calculated if the post-bremsstrahlung electron is detected, as seen in Eq. 2.2. The photon tagger uses a large magnet to curve the electrons away from the original beam line, with the photons' paths being undisturbed by the magnetic

field. The electrons are steered to the focal-plane detector, which is composed of a series of 353 overlapping plastic scintillators that activate when hit by a charged particle. An electron's radius of curvature can be determined with

$$r = \frac{p}{qB}, \quad (2.3)$$

where p and q are the electron's momentum and charge, respectively, and B is the given magnetic field [Tip08]. Therefore, electrons with a lower momentum will be bent toward the lower portion of the focal plane, while the more energetic photons will have a large radius of curvature and hit further up on the focal plane. The tagger is calibrated such that the position of the activated scintillator gives the electron energy. Since the distances involved with the tagger and target detector set-up are very well known, timing coincidences may be used to pair an event in the target detected by the CB/TAPS set-up with the electron that produced the photon responsible for that event. Naturally, not all electrons will radiate. The ones that did not produce a photon do not lose any energy, and their radius of curvature is much larger. These electrons are directed into the beam dump. The Glasgow Tagged Photon Spectrometer is shown in detail in Figure 2.6.

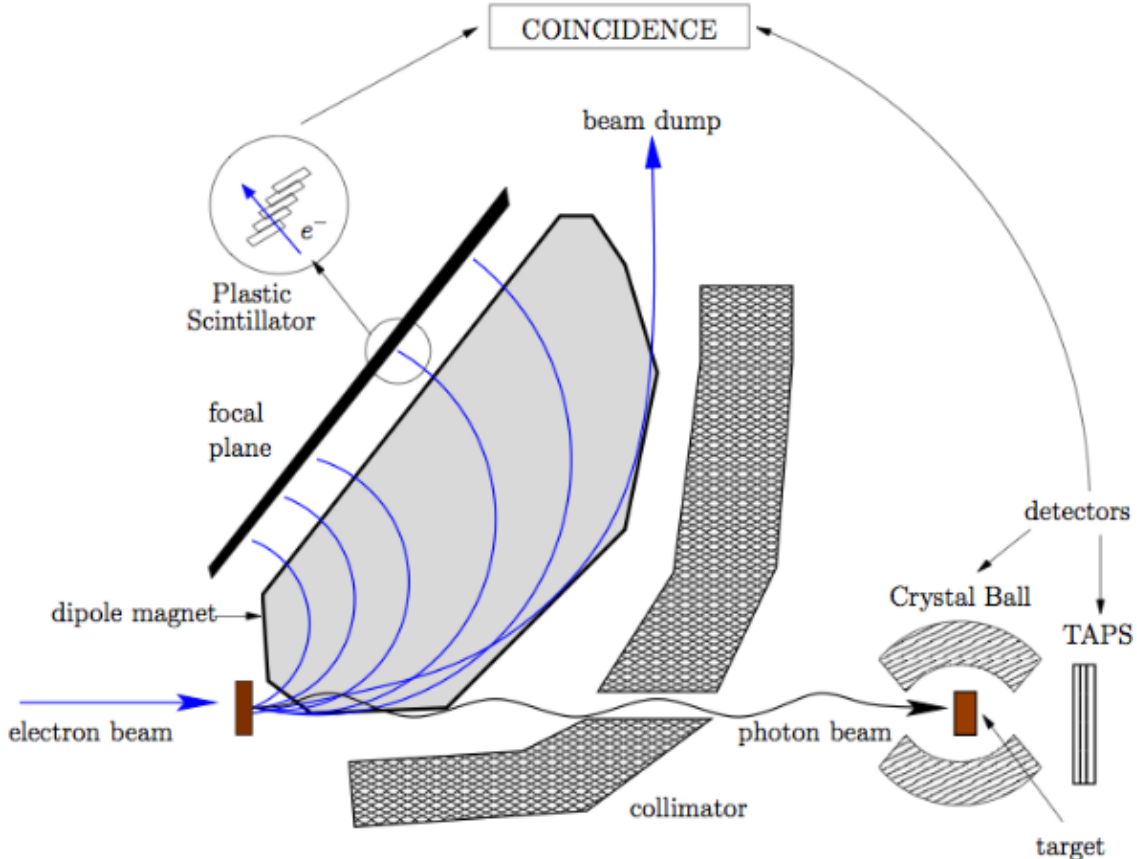


Figure 2.6: The electron beam path through the radiator (shown as a brown rectangle on the left) to the Glasgow Tagged Photon Spectrometer. The photon beam path to the target along with the detector set-up around the target is also shown.

2.2.3 Target

The photon beam is then incident upon the target, where it scatters off of stationary nuclei contained within the cell. This scattered photons have energy $E_{\gamma'}$ and are detected by the CB/TAPS detectors, detailed in Section 2.2.4 and 2.2.5. The target that motivates this work, the Active Helium Target, is described in great detail in Chapter 3.

2.2.4 Crystal Ball

The Crystal Ball (CB) is the predominant detector in scattering events. Spherical in shape and composed of 672 thallium-doped sodium iodide ($\text{NaI}(\text{Tl})$) crystals, the CB covers 93% of the 4π steradians solid angle around the target [Hor19]. The CB allows for polar (θ) angle coverage from 20° to 160° and full azimuthal (ϕ) angle range. Each scintillating crystal is coupled to a photomultiplier tube, which transmits a signal to an analogue-to-digital converter (ADC) and a time-to-digital converter (TDC). The CB has an energy resolution of $\Delta E/E = 0.020 \times E[\text{GeV}]^{0.36}$ [Tho16]. As it was originally constructed at the Stanford Linear Accelerator in the 1970's for collision experiments, the CB has a large gap in the forward and backward regions [Tho16]. While the front entrance point is still necessary for the A2 Collaboration's photon beam, the hole at the back did cause a problem. Fortunately, the TAPS detector was used to compensate for this loss of coverage in the forward direction.

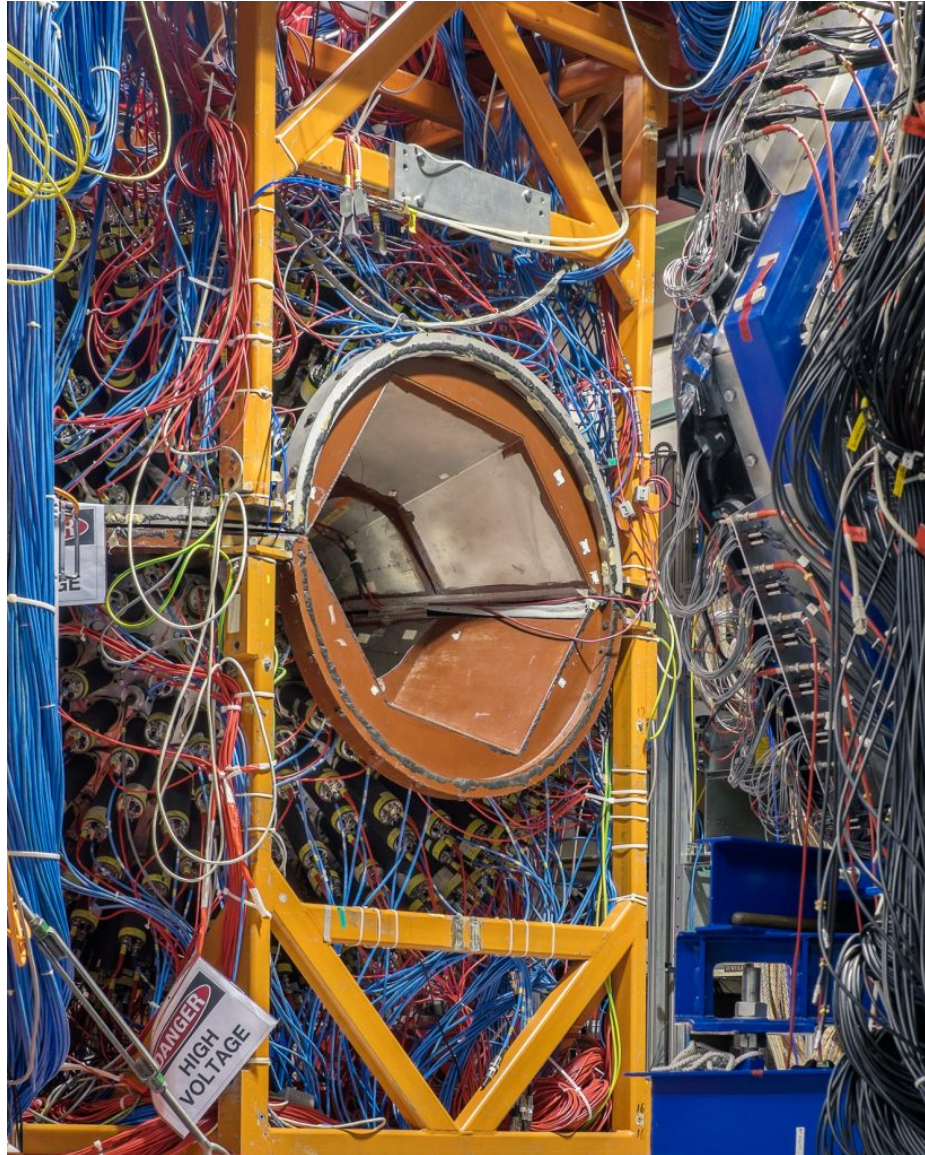


Figure 2.7: The Crystal Ball detector in the A2 Hall. The opening where some angular coverage is lost can be seen along with the PMTs and high voltage modules [MAM21].

2.2.5 Two Armed Photon Spectrometer

In the forward direction, the detector set-up is completed with the Two Armed Photon Spectrometer, or TAPS. An array of 366 barium fluoride (BaF_2) crystals and 72 smaller lead tungstate (PbWO_4) crystals are positioned together in a honeycomb

pattern to form a hexagonal wall, as seen in Figure 2.8. The PbWO_4 crystals are strategically positioned in the center of the wall where the most hits occur, since they are capable of rapid scintillation. These form the two inner white rings seen in Figure 2.8. Each crystal is coupled to a PMT, which then feeds the signal to an ADC and TDC. TAPS is also equipped with a layer of plastic veto tiles, which gives the ability to discern between charged and neutral particles.

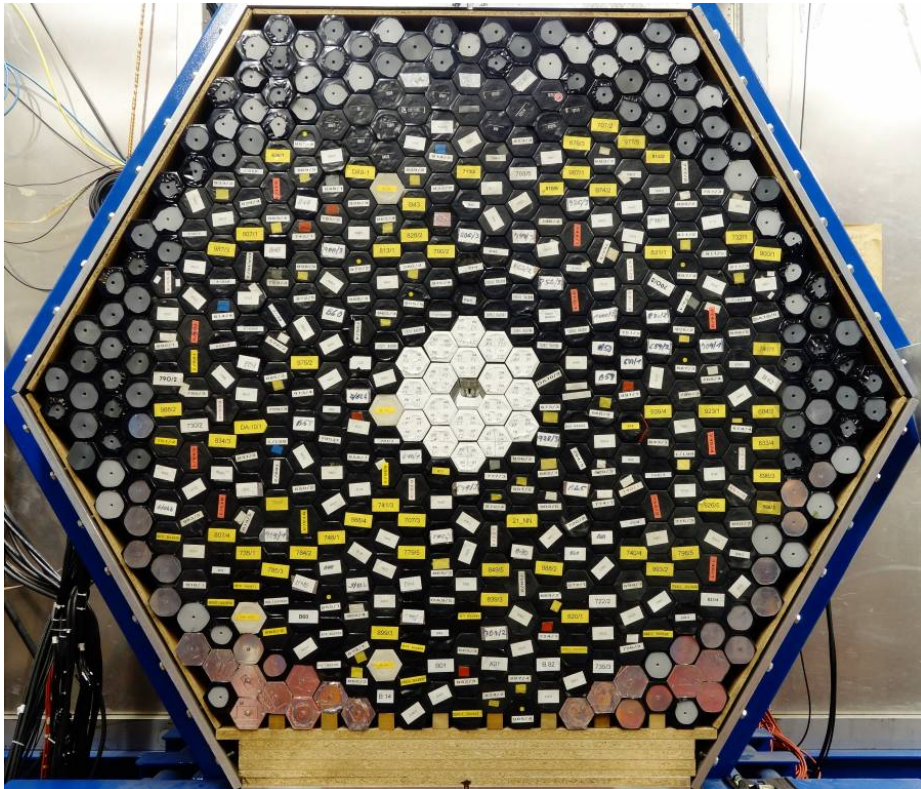


Figure 2.8: During an experiment, TAPS is placed close to the Crystal Ball to achieve necessary coverage; however this is a picture of the TAPS isolated.

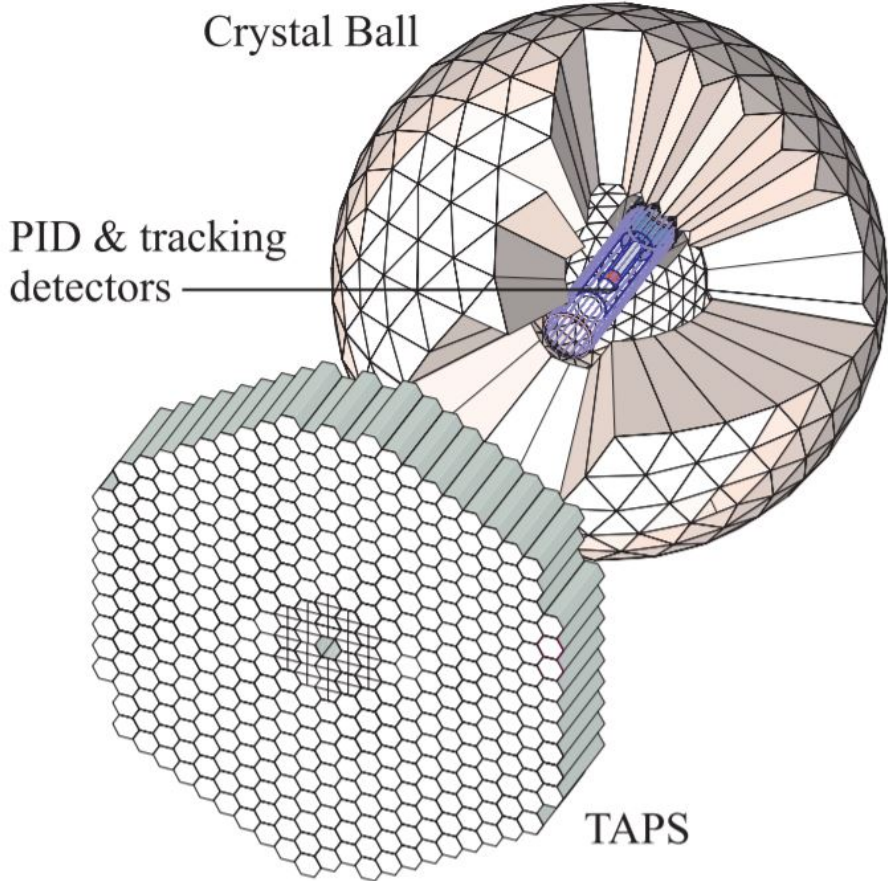


Figure 2.9: Visualization of the CB-TAPS detector set-up in Mainz. The beam line enters the CB from the top right-hand side and passes through the target cell, shown here surrounded by the PID and tracking detectors in the center of the CB [Hor19].

2.3 Monte Carlo Simulations

An integral part of this thesis is the use of simulations in the analysis procedure. Simulations provide physicists with the ability to not only test the experimental setup, but also to make parameter changes that would otherwise be very difficult to implement. Monte Carlo (MC) methods are powerful tools in modelling the probability of different outcomes that cannot easily be predicted due to random variables. By generating random events that fit within certain constraints, it is possible to observe

the probability distribution of different results. In this case, the particle interactions due to the incoming photon beam on the target are modelled. EvGen, the stand-alone MC program, and Geant4 are the three software tools used in the analysis for this experiment.

2.3.1 Event Generation

The first step in simulating data is to generate the initial events. Event Generator, or EvGen, is the program used to produce the scattering data. Written in C++ by Dr. D.L. Hornidge, it uses a MC reaction kinematics generator to output the resulting momenta and energies of scattered particles [Hor20]. The program necessitates the input of certain parameters such as number of desired events, incident photon energies, target material, and reaction type. The output is a ROOT file that can then be used in either the standalone MC code or by Geant4. The histograms in the ROOT file may also be examined individually to examine the recoil particle energy distribution, for example. Developed by CERN, ROOT is a data processing framework commonly used in high energy particle physics [CER21a].

2.3.2 Standalone Monte Carlo Program

The standalone MC program, written in C++, is capable of generating random events within the target volume. Rather than looking at the scattered photons, this code focuses on the recoil nucleus and its subsequent scintillation. The program produces an arbitrary number of recoil ${}^3\text{He}$ nuclei and follows the photons emitted by each nucleus to see if they are detected. Instead of creating events with random energy, it can also take an EvGen output file as input. This allows for the recoil nuclei to follow the energy distribution simulated by EvGen, giving more accurate results. This code was written by the author specifically for testing new wavelength shifting geometries

in the active target.

2.3.3 Geant4

The files from EvGen may instead be passed into Geant4 for a more rigorous analysis. Geant4 (**G**Eometry **A**ND **T**racking) is a C++ object-oriented MC toolkit used for the simulation of particles passing through matter [CER21b]. Developed by CERN, it is suitable for this analysis due to its ability to accurately model optical photon transport. A version of Geant4 has been written to track the particles from EvGen all the way through the AHeT and the detectors in the A2 Hall. The output from A2Geant4 is in the form of ROOT tree files containing information about the hits and energy detected by each detector. In this case, the important trees are the ones containing information about the energy detected by each SiPM.

Chapter 3

ACTIVE HELIUM TARGET

The Active Helium Target (AHeT) is the name for the target containing pressurized gaseous ^3He or ^4He . As mentioned in Section 2.2.3, the vessel is to be placed directly in the CB inline with the photon beam, with Compton events occurring in the active volume. Once built, the data obtained from the AHeT will ultimately allow for the neutron scalar polarizabilities to be extracted with lower uncertainties.

3.1 Active Component

Compton scattering off of helium nuclei will occur in the target volume following the process outlined below,



where γ is the incident photon, He is the initial helium nucleus, γ' is the scattered photon, and He' is the recoil nucleus. The helium nucleus before a scattering event is assumed to be at rest. When examining the data obtained from a beamtime in the A2 Hall, it is important to discern backgrounds from actual Compton scattering events. This may be done by examining the initial and final states of each of the particles involved. The following kinematic constraint,

$$E_{miss} = E_\gamma - E_{\gamma'} - E_{\text{He}'} = 0 \quad (3.2)$$

may be used to perform data cuts in the analysis stage, where events that possess this signature when reconstructed are identified as Compton events. Here, E_{miss} is

the missing energy and should be zero by conservation of energy, E_γ is the incoming photon energy which is known from the tagger, and $E_{\gamma'}$ is the scattered photon energy which is obtained via the CB-TAPS setup. However, the recoil helium nucleus does not have enough energy to exit the target cell in the vast majority of cases. This means that one piece of the puzzle, $E_{He'}$, is missing. Fortunately, after getting hit by an energetic photon, the helium nucleus recoils and deposits its kinetic energy, $E_{He'}$, in the surrounding gas. As the now excited helium atoms de-excited, they emit scintillation light predominantly in the vacuum ultraviolet (VUV), with a peak at 80 nm (see Figure 3.1) [Jeb13]. This scintillation light does not make it out of the target, which means that the cell that contains the active gas must not only enclose the events, but also detect them. Collecting the emitted photons via silicon photomultipliers (SiPMs) would give the final piece to the missing energy puzzle, $E_{He'}$.

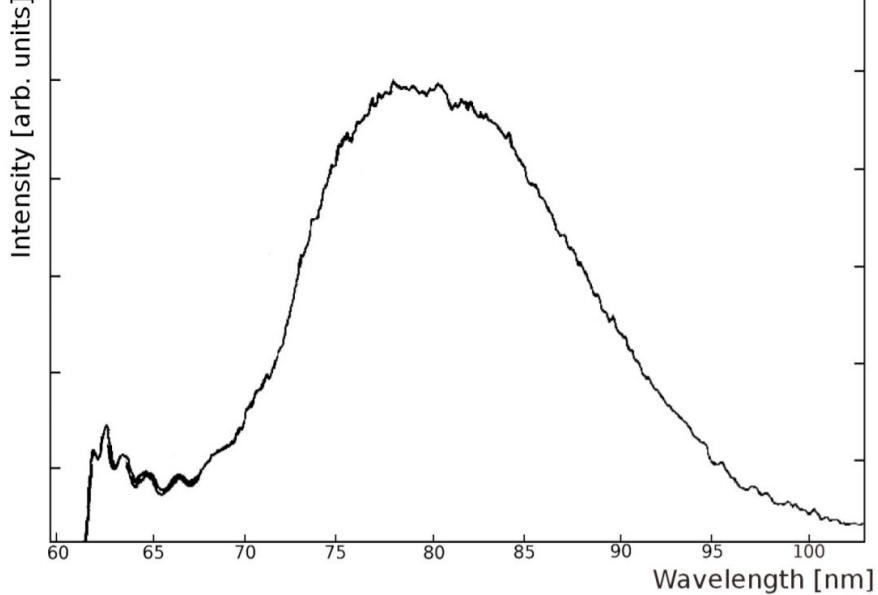


Figure 3.1: Ultraviolet emission spectrum of a high-pressure helium discharge lamp [Jeb13]. Helium scintillates primarily in the 70–95 nm range, with a peak at 80 nm.

Since no system will be 100% efficient at detecting all of the scintillation light, the success of extracting the total energy via scintillation light depends on two things. The first is whether there is a good relationship in the simulated data between the energy deposited in the target and the energy detected. The second is if the experimental results match the simulation. One way to test the second point is by placing an alpha particle source, which has a known energy, in the target, and comparing data from this with the simulation. If the two criteria are met, a calibration can then be established, where for each event, the amount of energy deposited in the target can be extracted. However, this energy calculation only works in the case of Compton scattering, and even then, it is likely that the helium energy will not be known with great precision. This energy can still be used as a kinematic cut, eliminating events that clearly deposited too little, or too much, energy in the target to be a coherent Compton scattering event.

A second advantage of an active target is the ability of vertex reconstruction. Since helium scintillates almost entirely at the point of interaction, the event position may be extracted by looking at which detectors in the target record a signal. Using the known placement of the detectors that register a signal, and the strength of those signals, the event vertex may accurately be determined. When the Compton scattered photon is detected in CB-TAPS, it is assigned a polar angle assuming a vertex at the origin. Since the target is 40 cm long, knowing the actual vertex enables a more accurate determination of the polar angle. [Mar21].

3.1.1 Scintillation Yield

Scintillation yield is defined as the number of photons emitted per unit of energy deposited, in MeV^{-1} . While the exact number of photons emitted per MeV of energy deposited by the helium nuclei in the pressurized gas is not well covered in the lit-

erature, we may turn to other works to obtain an estimate. Fortunately, most noble gases are fairly good scintillators and are extensively used in experiments for particle detection. Unfortunately, gaseous ^3He is not as commonly used as other elements, leading to less documentation [Ito13]. A paper published in 2012 by Chandra et al. found that approximately 18 000 VUV photons are produced per MeV of energy deposited by neutrons in 200 bar ^4He [Cha12]. Furthermore, a 2013 paper by Ito et al. found the number of UV photons produced by an alpha particle stopped in liquid helium, plotted in Figure 3.2 [Ito13]. However, these are results for helium at extremely high pressure or in a liquid state. The experimental results that best approximate the AHeT conditions are from Al Jebali (2013), where the scintillation pulse height of helium mixed with 500 ppm of nitrogen is investigated. It found that \sim 100 photons/MeV were emitted at 1 MPa and \sim 60 photons/MeV were emitted at 2 MPa [Jeb13]. Although the target is to be at a pressure of 2 MPa, nitrogen is no longer being implemented as the WLS (see Section 3.4). The AHeT simulations must therefore consider several scintillation yields to account for the uncertainty. This work looked at yields of 65, 650, and 6500 photons to cover the full range of possibilities.

3.2 Design

While yet to be built, much work has been dedicated to advancing the AHeT design such that the ^3He scintillation light may be adequately collected. Many changes have been made to the AHeT design over the years, all of which will be outlined in the following sections. The current vessel design follows the Glasgow target with the wavelength shifter (WLS) component and SiPM placement still undetermined. Designing and simulating new WLS geometries for the target were the focal point of this work and are outlined in the last three sections of this chapter. These geometries adhere to the Glasgow design cell dimensions.

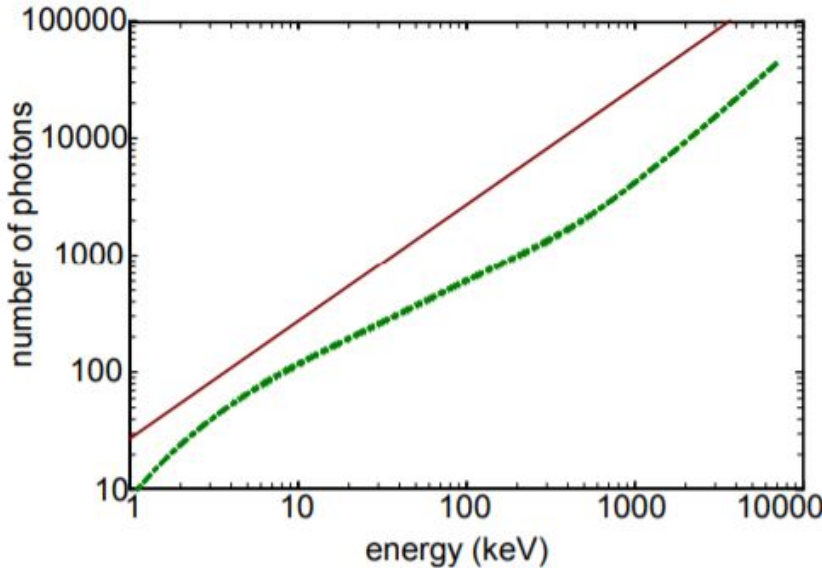


Figure 3.2: Number of prompt UV photons produced by primary particle stopped in liquid helium. Dashed green line: helium atom recoil (alpha particle). Solid red line: electron [Ito13].

3.2.1 Max-Lab Design

It was initially proposed to repurpose a target from MAX-lab in Lund Sweden that was previously used to measure photodisintegration cross sections of few-body systems [Jeb13]. This target, called the Helium Gas-Scintillator Active Target (HGSAT), consists of four main cells made of solid Al alloy, as shown in Figure 3.3. Each cell is optically isolated by $5\ \mu\text{m}$ thick aluminized mylar windows and is coupled to four photomultiplier tube (PMT), with a 10 mm thick synthetic quartz window separating the gas from the PMT. Attached to either end of the target are two additional cells with beryllium windows used for background reduction, with each cell coupling to a single PMT. In total, this amounted to 18 PMTs and a target length upwards of 30 cm. The gas is at a pressure of 2 MPa [Jeb13]. However, this target was not designed with scattered photon in mind and although it is quite wide, it is too small to fit within the CB without suspension. There were also some potential problems with

the certification of this apparatus for high-pressure operation since it has issues with the pressure retaining couplings [Ann14]. It was therefore decided that the benefits of an already built target did not outweigh the cons that accompanied it, and a new design was therefore necessary.

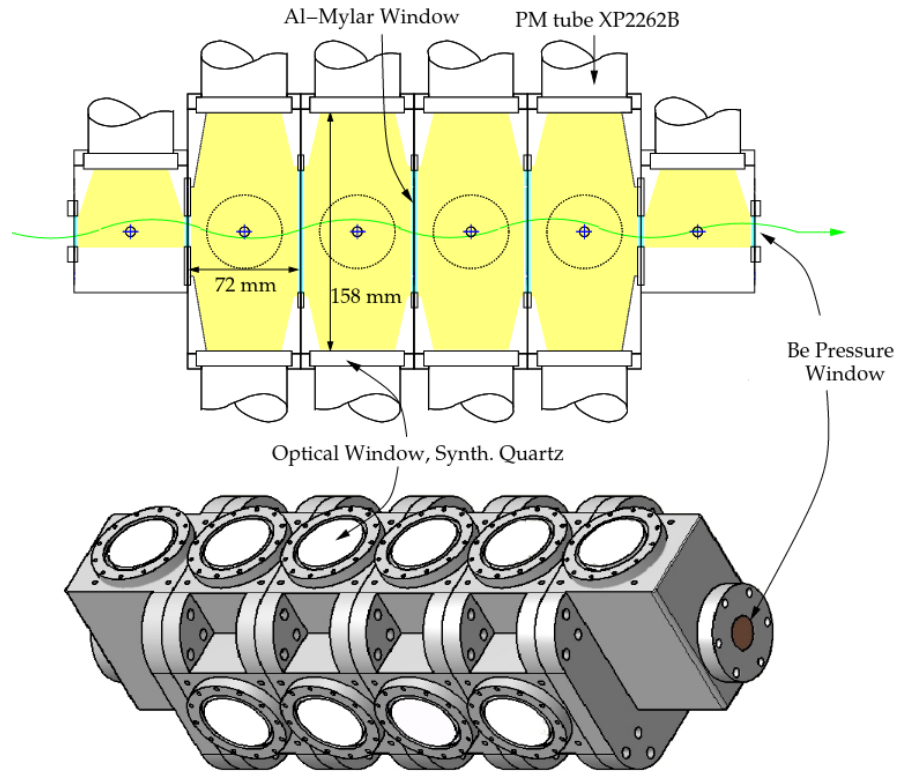


Figure 3.3: Schematic drawing of the original MAX-Lab Helium Gas-Scintillator Active Target (HGSAT).

3.2.2 Glasgow Design

The new design, put forward by Dr. J.R.M. Annand from the University of Glasgow in 2014, is shown in Figure 3.4 and will be referred to as the “Glasgow” design in this work [Ann14]. In total, the target is 80 cm in length; 40 cm of active volume plus 20 cm extension tubes on either end. The extension tubes have the purpose of isolating

the beryllium windows from the active volume in order to reduce background data. The main body of the target is a cylindrical cell made of aluminium alloy 5 mm thick and has an inner diameter of 102 mm. The 2 cm in diameter beam entrance and exit holes in the cell have aluminized mylar windows to help enhance optical isolation within the active volume by reflecting light. This also allows for a well defined “active volume”, i.e., the volume in which events occur. Finally, the cell is to be filled with helium gas at a pressure of 2 MPa. The high pressure is used to increase the effective target thickness and hence the Compton scattering event rate [Jeb13].

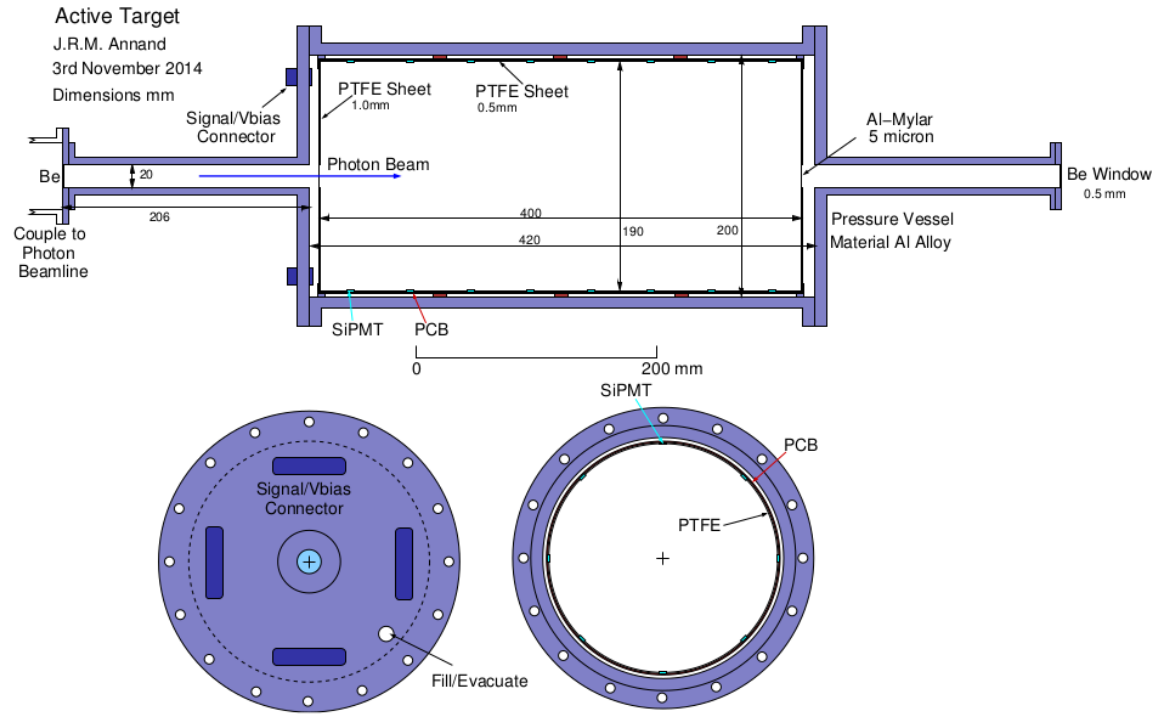


Figure 3.4: Sketch of Glasgow target, designed by D. J.R.M. Annand from the University of Glasgow. The main cylindrical cell is 40 cm in length and has a diameter of 102 mm, while the two extension tubes are 40 cm each [Ann14].

${}^3\text{He}$, like most noble gases, is a fairly good scintillator [Cha12]. The Glasgow design calls for silicon photomultipliers to be placed along the inner surface of the main cell to collect the helium scintillation light [Ann14]. As will be seen in more

detail in Section 3.2.3, the SiPM detect in the 200 – 900 nm range, with a peak detection efficiency (PDE) at 420 nm [Sen17]. This means that they are blind to the helium scintillation light, which has a peak emission at 80 nm [Jeb13]. Originally, nitrogen gas was meant to be added to the helium, since it was thought to effectively shift the VUV light to the visible region [Ann14]. However, further testing showed that nitrogen was insufficient as a WLS on its own (see Section 3.3.2).

3.2.3 Silicon Photomultipliers

The collection of scintillation light from scattering events will be accomplished with the use of silicon photomultipliers, as opposed to the PMTs used in the MAX-lab design. Employing SiPMs instead of PMTs circumvents the need for optical windows and their smaller size makes a more compact target design [Ann14]. SiPMs are similar to PMTs in the sense that they still use the photo-electric effect to convert photons to photo-electrons via an array of avalanche photodiodes [Sch21]. Photodiodes are formed by $p - n$ junction and function in a similar manner to solar cells [Sen17]. In the AHeT, the J-Series SiPMs from the company Sens-L will be employed [Mar21]. The J-Series sensors are 6 mm and use solid-state technology. As seen in Figure 3.5, these have a detection range of 200 – 900 nm, although they are most efficient at 420 nm [Sen17]. This means that the SiPMs are incapable of detecting the VUV scintillation light emitted in the target.

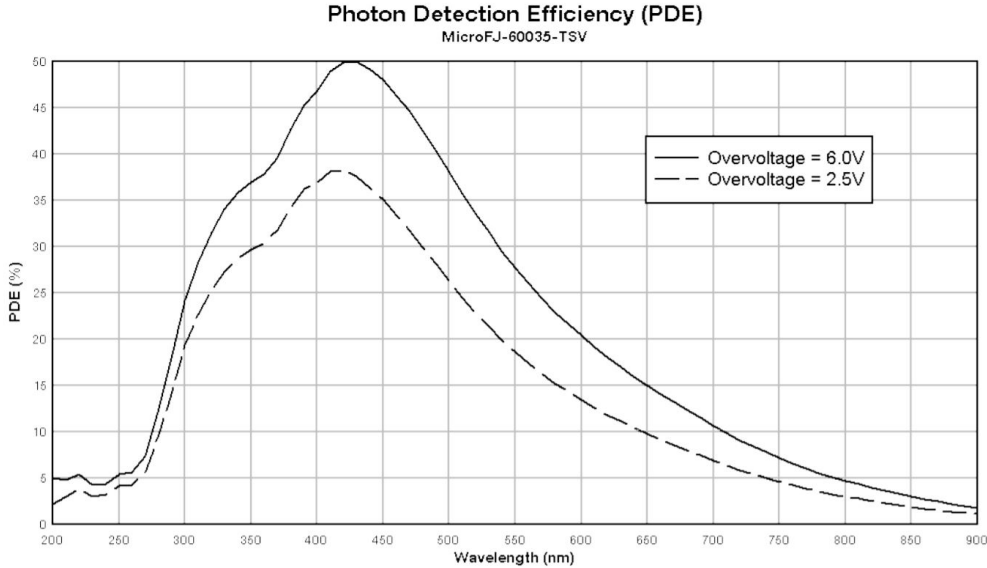


Figure 3.5: Detection efficiency of the Sens-L silicon photomultipliers to be employed in the AHeT [Sen17]. One can see that they are most efficient in the 200–900 nm range, with a PDE at 420 nm.

3.3 Prototype

Extensive WLS testing was completed on a prototype target in the summer of 2019 and is well documented in the 2020 honours thesis of M.S. Perry [Per17]. Contrary to the Glasgow design, the prototype had 20 cm of active volume containing helium at a pressure of only 1 MPa, and 20 cm of extension tube. This vessel is pictured in Figure 3.6. Since the goal was to test scintillation detection within the vessel, this modified design sufficed. To conduct experiments, the vessel was evacuated, filled with ${}^4\text{He}$ at a pressure of 1 MPa, and depending on the tests being run, also filled with 0.0015 MPa of nitrogen [Per17]. Seeing as it would not be feasible to use the photon beam produced in the A2 Hall for these prototype tests, a ${}^{241}\text{Am}$ source, producing 5 MeV α particles, was used to simulate Compton events. This is a reasonable approximation to actual events since α particles are simply energetic helium

nuclei. When an ejected α particle travels through the gas, it excites it in a similar manner to a recoiling helium nucleus after a Compton event.

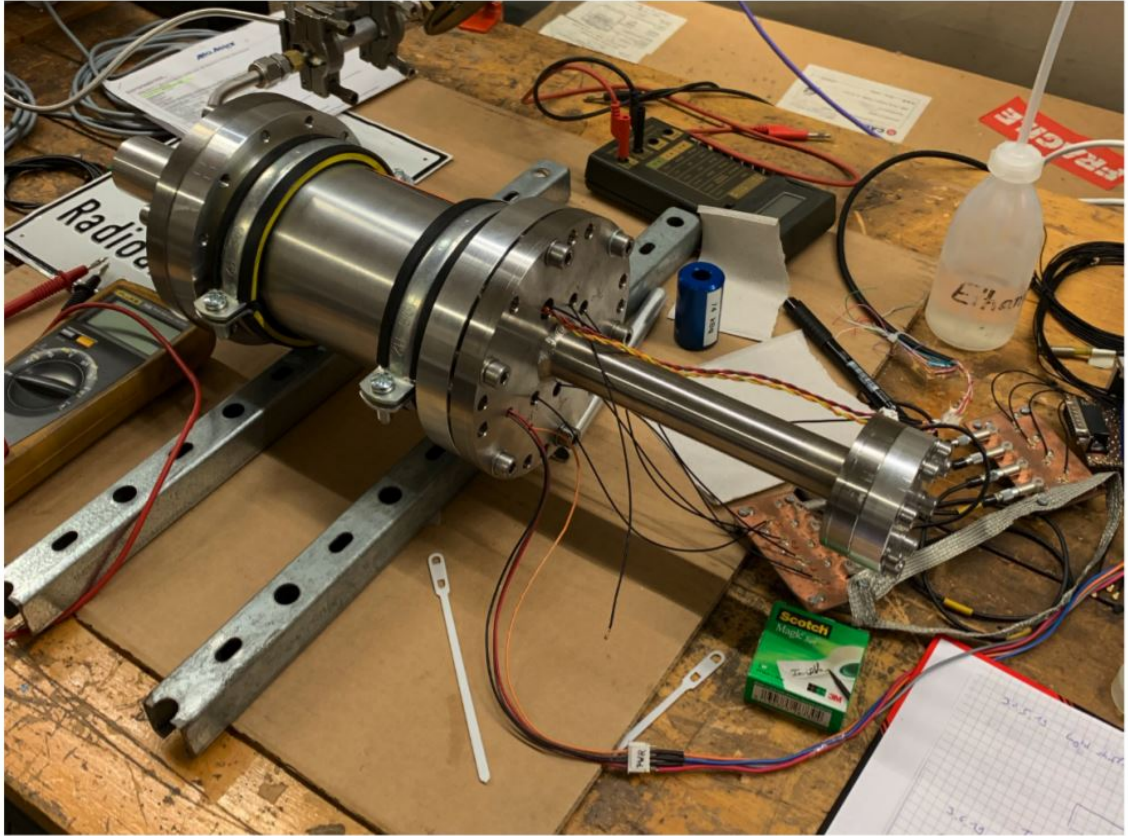


Figure 3.6: The prototype AHeT used for testing [Per17]. This was only 40 cm in length compared to the Glasgow design's 80 cm and suffered from reduced coverage.

3.3.1 SiPM Arrangement

Pictured in Figure 3.8 is the SiPM orientation in the prototype. Eight green 1 mm thick printed circuit boards (PCB) run down the cylinder axis, with each PCB having 18 6×6 mm SiPM diodes along its center. This amounts to 144 SiPM diodes in total. On each PCB, there are six channels, making three SiPMs per channel. The channel signal readout is given by an OR operation, meaning that the channel will record an event when any of the three diodes detect something.

All eight PCBs read the same six channels, with the three diodes in the same relative position tracking each channel. This is illustrated in Figures 3.7 and 3.8, where each coloured line represents a channel. Theoretically, this should allow for the position of an event to be recorded, since each channel covers a section of the cylinder axis [Per17]. However, the prototype suffers from reduced coverage. As can be seen from Figure 3.8, the SiPMs only cover a small portion of the inner surface are, which means that a considerable amount of the light would escape detection.

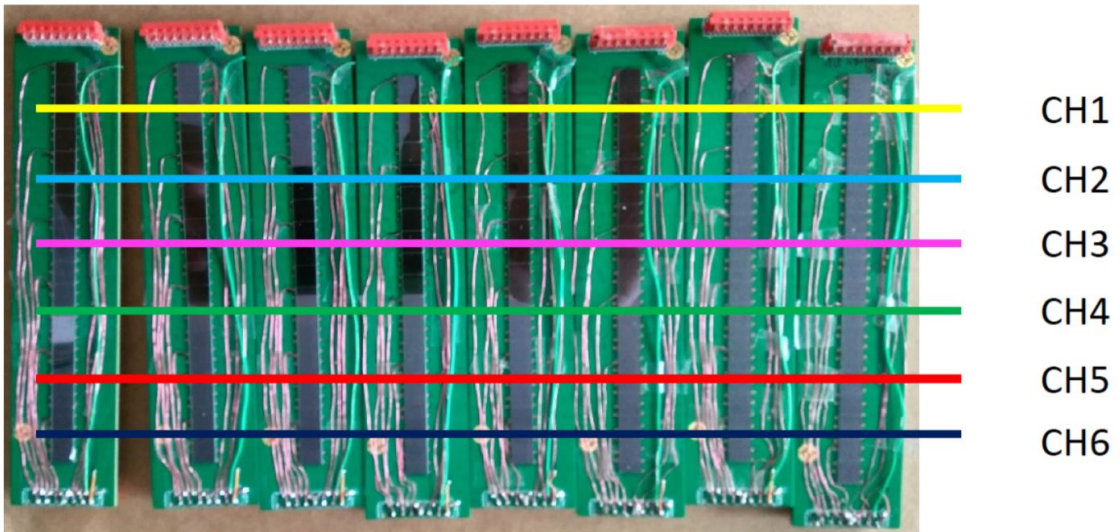


Figure 3.7: Pictured are SiPM diodes running down each of the eight PCBs. The channels follow the same colour scheme as seen Figure 3.8, with the first three SiPM diodes of each PCB are in channel 1, the next three are in channel 2, etc. [Per17].

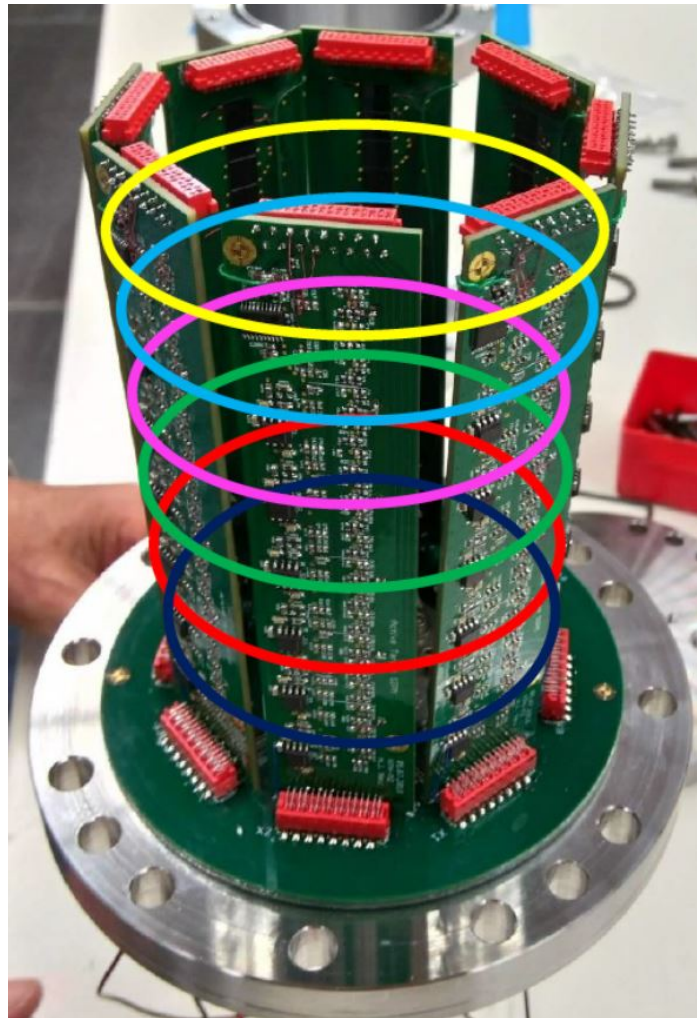


Figure 3.8: Pictured is the PCB arrangement within the prototype target, with each coloured ring representing a channel [Per17].

3.3.2 Test Results

Testing was conducted with nitrogen being added to the helium gas at 500 ppm and one PCB with three active diodes was used to collect data. The scintillation from a Compton event will shower the diodes with light, and so a signal was only considered to be an event when there was a coincidence between all the diodes. When the α particle source was placed directly on top of the SiPM, the signal appeared to be

successful. However, when the source was moved to the center of the cell to simulate more realistic events, the signal yield dropped significantly. It was therefore decided that nitrogen on its own would not be sufficient and that new methods must be explored [Per17].

3.4 Investigating Wavelength Shifting

While many alternative wavelength shifting avenues were explored, the most promising medium is the commonly used wavelength shifter tetraphenyl butadeine (TPB).

3.4.1 TPB

Often used in dark matter and neutrino detection experiments that employ noble gases, TPB is an organic compound capable of shifting the extreme ultraviolet scintillation light from the noble gases to visible light [Geh11]. TPB hosts several benefits. The first is that its properties are well documented in the literature. Detection of vacuum ultra violet scintillation light is a common challenge among research groups that use noble gases as scintillators seeing as commercial photodiodes are incapable of detecting such a short wavelength. Another benefit is its re-emission spectrum. As seen in Figure 3.9, TPB has a peak in re-emission at 420 nm, which is highly desirable seeing as the SiPMs have a PDE at 430 nm. This figure also shows no dependence of re-emission spectrum on incident wavelength [Ben18].

Finally, TPB may be coated on a thin film or acrylic light guide, the latter of which could cover a large surface area and funnel the light to the SiPM diodes. This helps solve the reduced coverage problem seen in the prototype. Instead of coated on, this compound may also be doped in materials, as seen in [Ada18], where TPB doped fibers are used in the DUNE experiment. Although such fibers are not commonly manufactured, they may be custom ordered from Saint-Gobain, a French company

that specializes in fabricating scintillating, wavelength-shifting, and light-transmitting fibers used in research and industry, among other things [Gob21]. The available fiber sizes range from 0.25 to 5 mm square or round cross-sections.

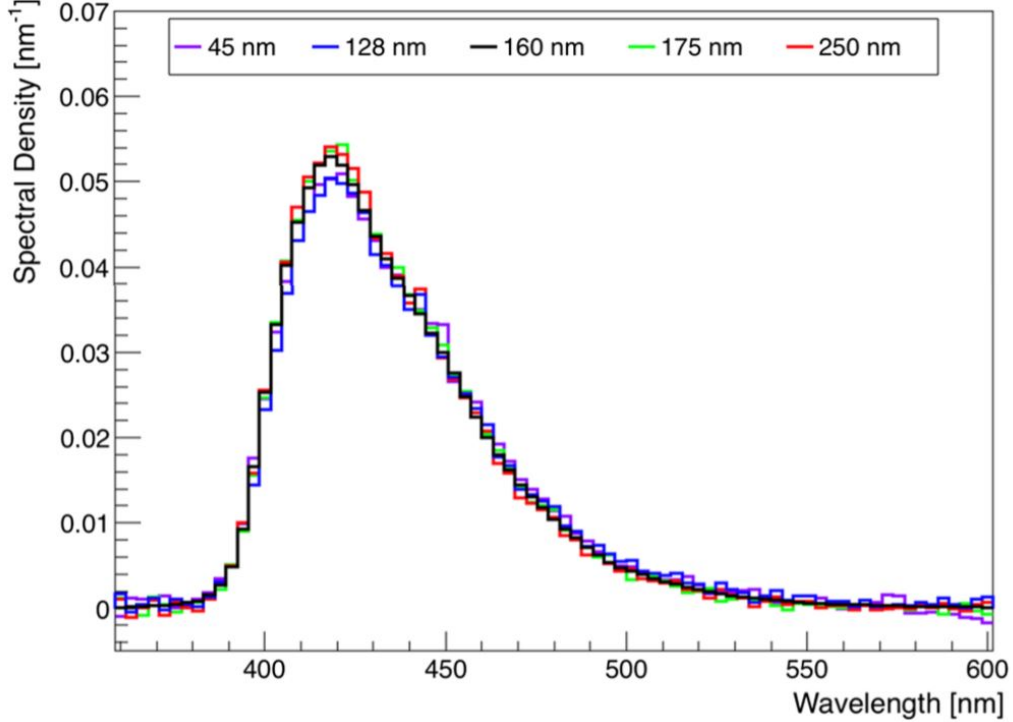


Figure 3.9: Re-emission spectra of a $1.8 \mu\text{m}$ TPB film for several incident wavelengths. No dependence on incident wavelength was observed [Ben18].

3.5 New WLS Designs

This work examines several new wavelength shifting geometries for the AHeT. The following section outlines the three designs: the acrylic lights guide, fiber barrel, and fiber helix designs. Each inner geometry uses TPB as the WLS and must accomplish several things. The first is that, ideally, the full inner area of the active volume must be covered with material or detectors such that no scintillation light escapes detection. The second is that the material used to capture this light must also shift it from the

VUV range to a longer wavelength compatible with the SiPMs. In other words, it must implement TPB. Finally, the material coupled to each individual SiPM must cover a large enough solid angle such that a meaningful signal may be read out by each diode. The target vessel dimensions and materials follow the Glasgow design, with the designs each having their own SiPM placement and WLS geometry.

3.5.1 Acrylic Light Guides

The first design is the acrylic light guide design. This employs trapezoidal acrylic light guides placed on each individual SiPM and a coating of TPB placed on the face of each trapezoid. These elements are highlighted in Figure 3.10. Custom shaped light guide geometries may be ordered from Saint Gobain [Gob21].

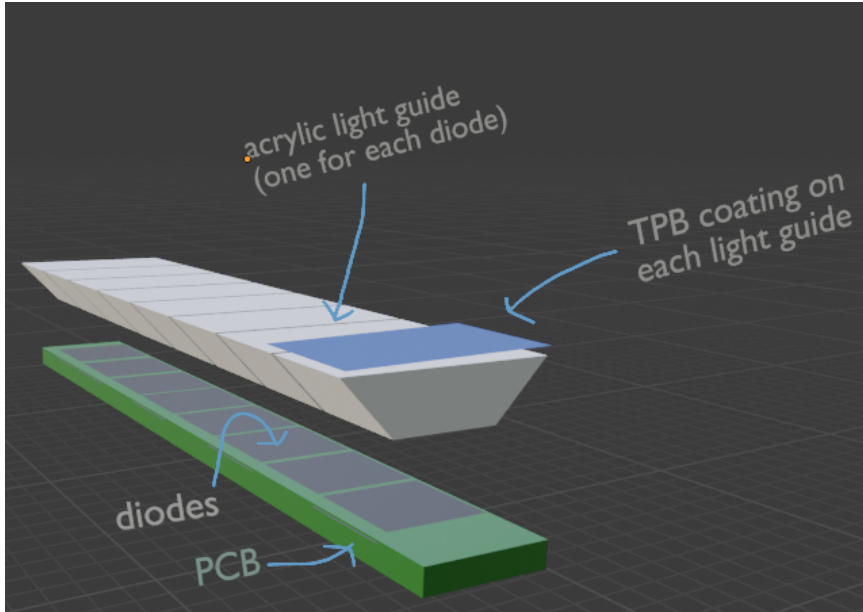


Figure 3.10: Pictured is a sample of the acrylic light guide design one PCB shown in green, the SiPM diodes shown in black, and the acrylic light guides on top of each SiPM shown in white. One TPB coating is drawn on the first light guide in blue.

The outside face of the light guide was 6×39.25 mm, and allows a larger azimuthal

angle coverage while also conserving the original PCB placement. Figure 3.11 shows the light guide geometry inside the target shell.

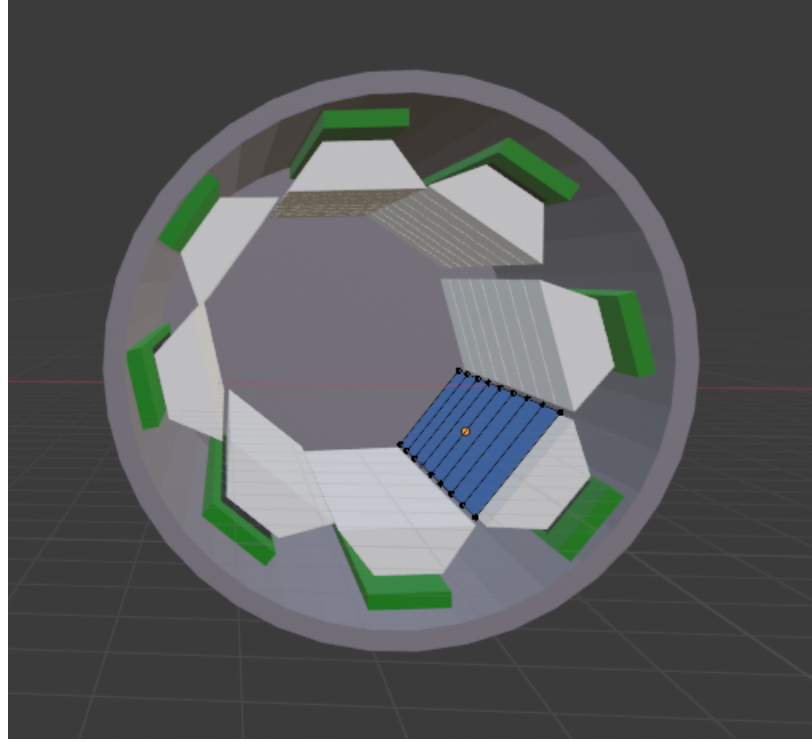


Figure 3.11: Acrylic light guide configuration in the target shell. For illustrative purposes, only one array of acrylic light guides is coated in TPB (blue), although all would be coated in practice. This drawing is not to scale.

3.5.2 Fiber Barrel Design

The fiber barrel design consists of TPB doped fibers run along the cylinder axis, as shown in Figures 3.12 and 3.13. Each 6 mm fiber connects to two SiPMs: one at either end of the target. This results in a ring of detectors at either end, as seen in Figure 3.12. When a photon is captured by a fiber, its wavelength gets shifted and the photon travels down the fiber via total internal reflection until it is incident upon a SiPM. With this design,

With TPB doped fibers, the output signal is affected by attenuation [Ada18].

Since the TPB doped fibers will have to be custom made, they do not currently have a data sheet. This means that the attenuation length used in the simulations is an approximate based on similar WLS fibers, which have attenuation length, λ , from 2 – 4 m [Kur21]. The attenuation is calculated using

$$I_z = I_0 e^{\frac{-z}{\lambda}} \quad (3.3)$$

where I_z is signal output at z , I_0 is the signal input, z is the distance travelled in the fiber, and λ is the attenuation length.

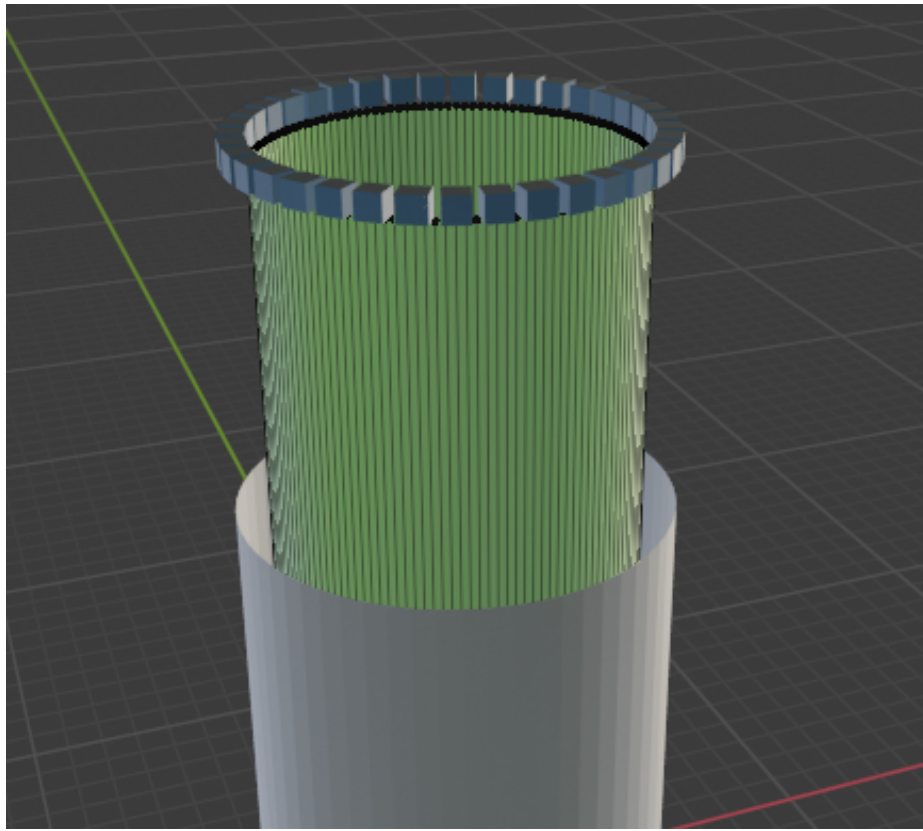


Figure 3.12: The barrel design in the target shell with one ring of SiPMs shown at the top. The TPB doped fibers, in green, are also shown. It is important to note that this is not exactly to scale, contrary to the Geant4 drawings.

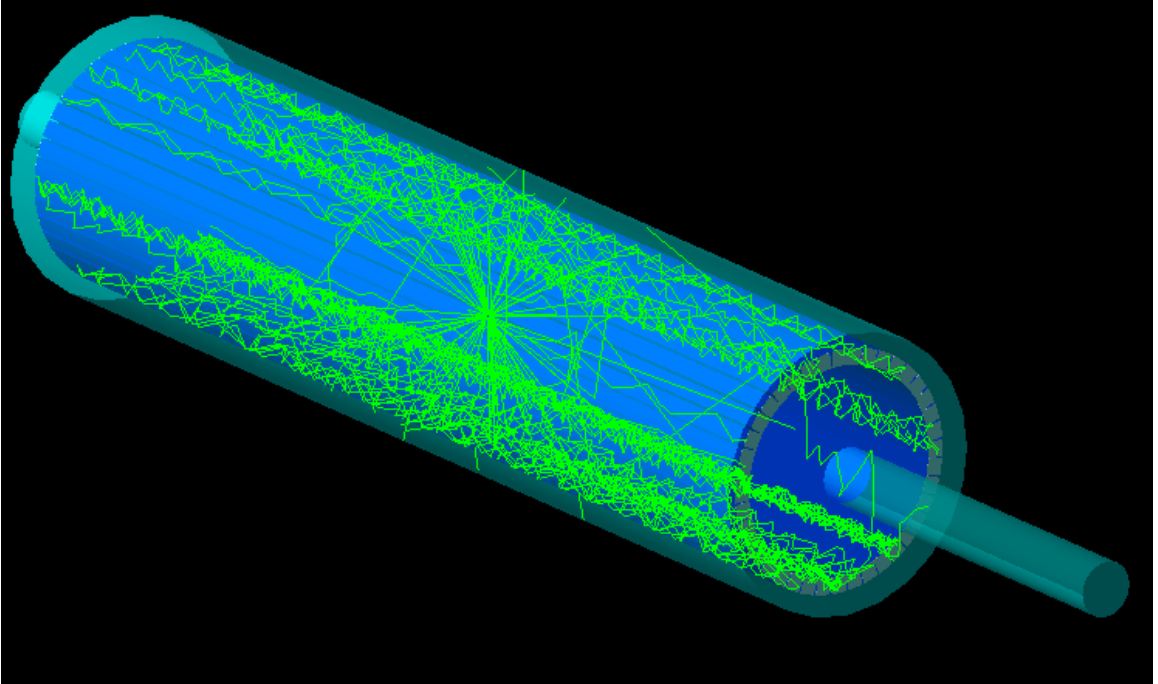


Figure 3.13: Geant4 rendering of the barrel design, with the fibers in blue and the scintillation photon trajectories in green. The scintillation light shown in this figure is the result of a 1 MeV alpha particle being thrown in the barrel design.

3.5.3 Fiber Helix Design

The helix design consists of 0.5 mm fibers wrapped 12 times into a spiral. This amounts to a 6 mm wide “ring”, as seen in Figure 3.14, that is each helix. After completing the wraps, each end of the fiber is lead to either end of the target where an array of SiPMs is located. When a photon is incident upon a fiber, it travels in the fiber via total internal reflection until it reaches a SiPM. The photons in the helix will travel up to 3.8 m for 12 windings, which is an appreciable length. This leads to a more significant attenuation of the signal. This design does offer the advantage of vertex reconstruction. The event position may be extracted by looking at which rings, and so which SiPMs, in the target record a signal. Using the known placement

of the rings that register a signal, and the strength of those signals, the event vertex may be determined.

The minimum bend radius increases as the fiber increases in cross section. A 0.5 mm fiber has a minimum bend radius of roughly 2.54 cm, while a 1 mm square fiber has a minimum bend radius of 5.08 cm [Mar21]. Therefore, to ensure that there is no cracking, the helix design is limited to the 0.5 mm width. More wraps could compensate for this constraint, allowing each diode to cover a larger effective solid angle. However, more wraps leads to a larger attenuation, which is undesirable.

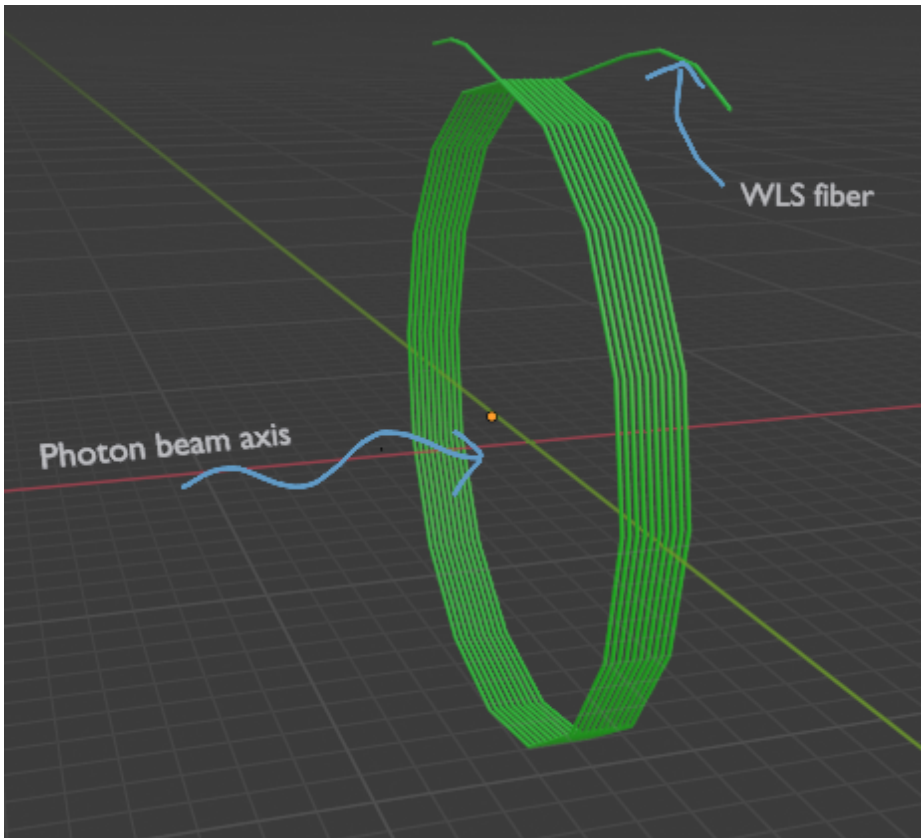


Figure 3.14: A sample of one helix with the photon beam axis following the blue arrow.

A possible design modification that circumvents the attenuation problem is achieved by replacing the helices with equivalent 6 mm long rings composed of 12 0.5 mm fibers.

This can be seen in Figure 3.15, where each ring has a small cut made in it along the z-axis, with each side of that coupled to a SiPM. The bright line along the cylinder axis represents the slice and placement of the SiPMs. The ring design was initially used as an estimate to the helix design, since the helix geometry was difficult to code into Geant4. However, the ring idea proved to be useful on its own.

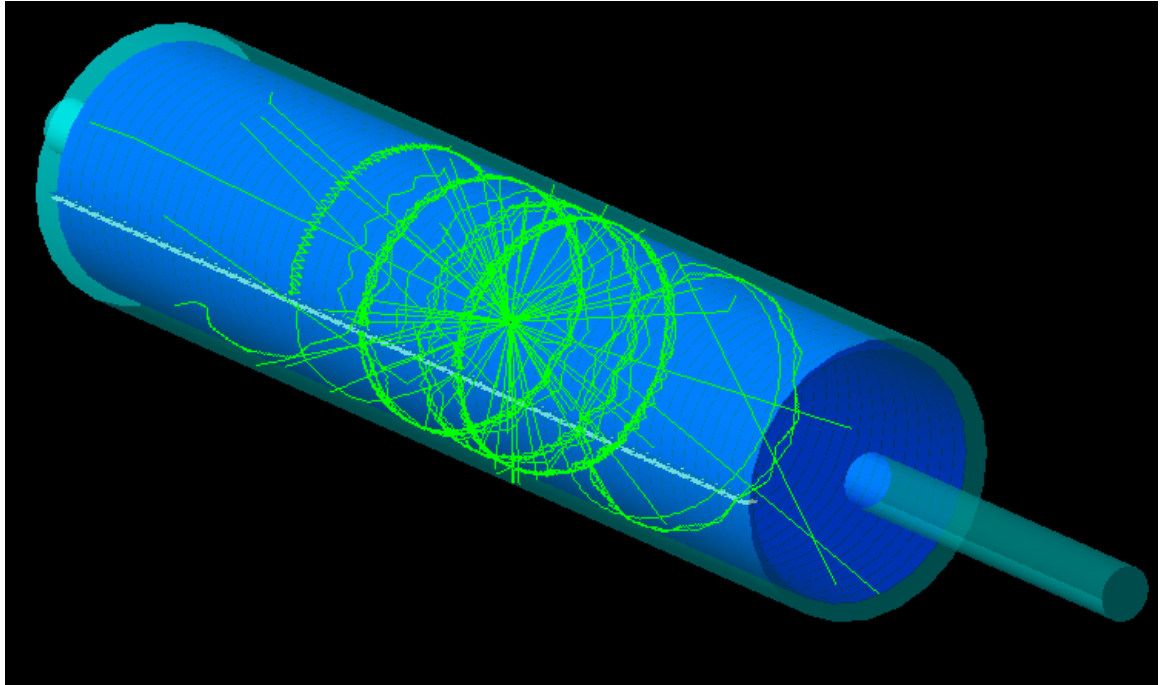


Figure 3.15: A drawing of the helix design from Geant4. This shows the ring design, used to approximate the results that would be obtained by the helix design. The bright line along the cylinder axis represents the SiPMs. The scintillation light shown in green is the result of a 1 MeV alpha particle being thrown in the target.

Chapter 4

ANALYSIS OF NEW DESIGNS

Three new designs were considered in this work. However, before physical testing may be completed with the new WLS geometries, simulations must be carried out to measure the feasibility of each idea. The simulations allow for the designs to be refined or changed without having to purchase new materials and assemble new geometries. This means many setups may be tested in a short period of time and at no cost. The following section outlines the software used in the data analysis as well as the success of each design.

4.1 Simulations

Studying the scintillation light yield was a multi step process. EvGen, standalone MC code, and A2Geant4 were the three tools used to simulate the physical processes for this experiment, explained below. While the light guide design was only analyzed with the standalone MC code, the full geometry of the barrel and helix designs were also coded in A2Geant4. This allowed for a more in depth analysis of the important particle interactions that would occur in the actual AHeT.

4.1.1 EvGen

The initial step in simulating data is creating the initial conditions of the kinematic event. As described in Section 2.3.1, for randomly generated kinematic processes, EvGen returns the final state of the particles. The files EvGen produces may be passed into the standalone MC code or A2Geant4. Depending on the recoil energies

| Process | Interaction | Energies (MeV) |
|-----------------------------------|---|----------------|
| Coherent Compton Scattering on He | $\gamma + {}^3He \rightarrow \gamma + {}^3He$ | 100, 150, 200 |
| Neutral Pion Production | $\gamma + {}^3He \rightarrow \pi^0 + {}^3He$ | 150, 200 |

Table 4.1: Summary of the main processes and energies considered with EvGen.

of each event specified in the file, scintillation light will be produced. A target length of 40 cm was specified for all runs seeing as the future target will have the same active volume length. Table 4.1 summarizes the energies and processes run in EvGen.

4.1.2 Standalone Monte Carlo Code

Written in C++ by the author specifically for this work, the standalone MC code provides preliminary scintillation yields for each design. The program generates a random number of Compton events within the target volume, each with a specified initial x , y , and z position in mm (see Figure 4.1). These event are distributed isotropically within the cell volume, which is not necessarily the case during an actual experiment. In fact, during a beam time, the events would most often occur in the beam line, which has a diameter much smaller than that of the target. Each of these events then give off an isotropic blast of photons, as seen in Figure 4.2. The program makes two main assumptions. First, it assumes that 65 photons are emitted per MeV of energy deposited by the recoil nucleus. Second, it makes each event scintillate entirely at the point of interaction. An EvGen file is then used as input to define the energies of the recoil 3He nucleus for each event. The plots shown in this thesis use an EvGen file for Compton scattering of 3He with a photon beam energy of 150 MeV as input. Then, each event emitted a number of photons according to:

$$\# \text{ photons emitted} = 65 \times E_{\text{recoil particle}}. \quad (4.1)$$

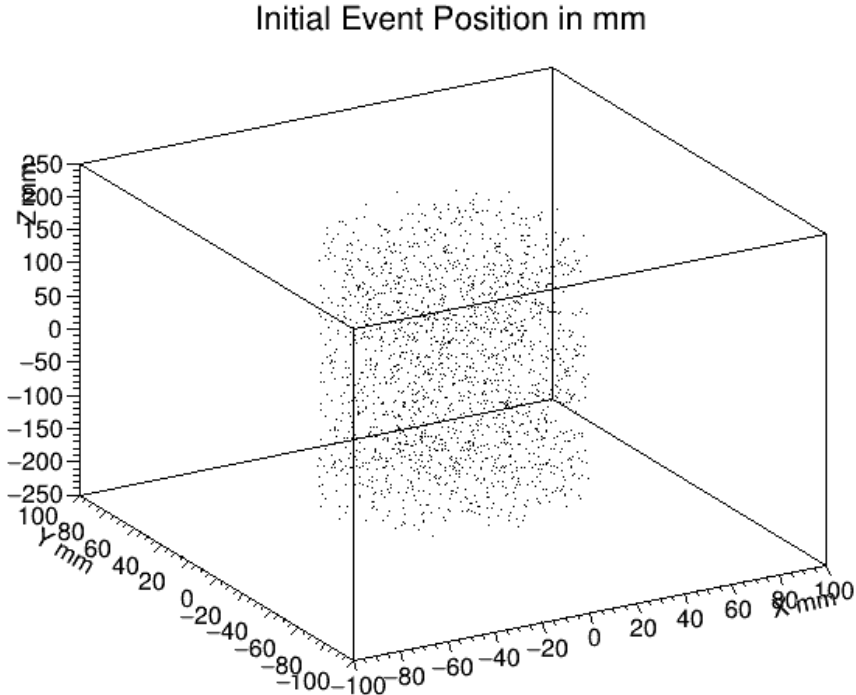


Figure 4.1: The initial position of each event as defined by the standalone MC program, shown as black dots. This is an example of 2000 events distributed isotropically in the target volume.

It was then possible to model the trajectory of each photon produced to see whether it would hit a “sample” of the WLS geometry for each design. For our purposes, one sample was defined as the amount of material or geometry that leads to one SiPM diode. The attenuation for both fiber designs was calculated using Eq. 3.4 and assuming an attenuation length of 400 cm.

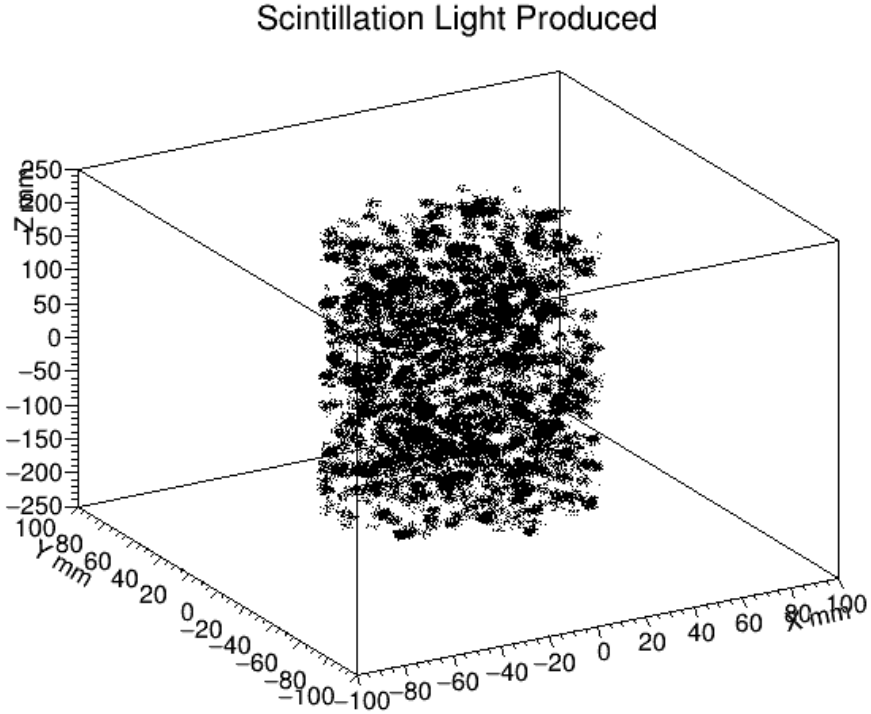


Figure 4.2: The blast of photons produced by each event, with each photon having a specified trajectory. This is an example of 2000 events distributed isotropically in the target volume.

4.1.3 A2Geant4

A2Geant4 is a software tailored to the A2 Collaboration's research. It is capable of simulating the complex particle interactions that take place in an actual experiment and was used as a more in-depth method of analysis compared the MC code. A4Geant4 is set up such that it takes the information provided by the EvGen file and matches up the particles that are being tracked. A specific type of files called .mac is used to tell A2Geant4 what to look at. For example, it could tell A2Geant4 to throw some particle at some energy and angle range and look at the scintillation output, or it could read in an EvGen file and analyze it. These macros can also be used to specify the detector setup. In the case of the AHeT, new parameter files were written

by Dr. John Annand from the University of Glasgow and Dr. Phil Martel from the A2 Collaboration to input the target dimensions and new WLS design geometries.

A2Geant4 outputs root files containing the detector results. For example, when 5 MeV α particles are thrown in the barrel design, the output plots include the two shown in Figure 4.3. The histogram on the left is the resulting energy deposited in each SiPM per throw. Since the WLS photons have a distribution of energies, there is a peak at about 3 eV for a SiPM detecting one photon, a second peak at 6 eV for an SiPM detecting two photons, etc. If the histogram on the left is then divided by the mean energy for each WLS photon, which is 2.875 eV, the graph on the right is obtained. This is the number of hits per SiPM per event. This process was followed for the fiber and helix designs to analyze the number photons per SiPM.

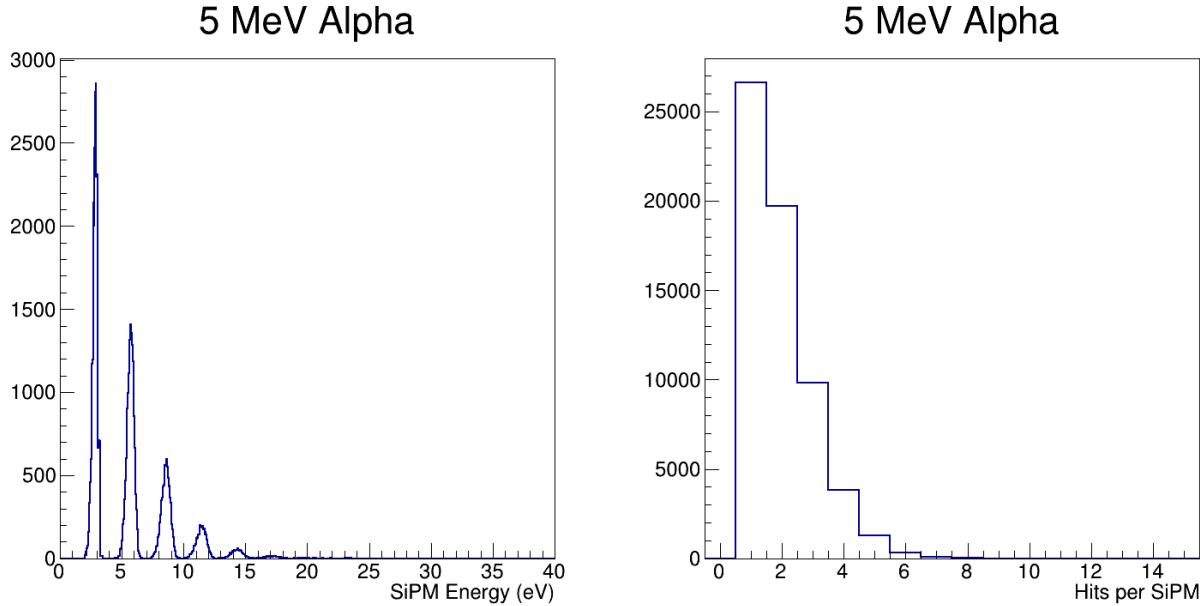


Figure 4.3: Energy deposited in the SiPMs per event (left) and the hits per SiPM per event (right).

4.2 Results

A summary of the mean hits per SiPM for each process run in A2Geant4 is tabulated in the Appendix. The means cited in the tables are not the raw histogram mean, but the mean of the median of hits per SiPM per event. A detailed explanation of the involved calculations is outlined in Section [A.1](#). The acrylic light guide design is not included in these tables since it was not simulated in A2Geant4.

4.2.1 Acrylic Light Guides

Standalone Monte Carlo Code

Figure [4.4](#) shows the number of successful scintillation photons per Compton scattering event. In this case, the sample geometry was defined as one 6×39.25 mm acrylic light guide. While physical properties that would diminish the signal, such as reflection, were not taken into account, the photon output was still quite low, with a mean value of 4.60. This design was therefore not further considered.

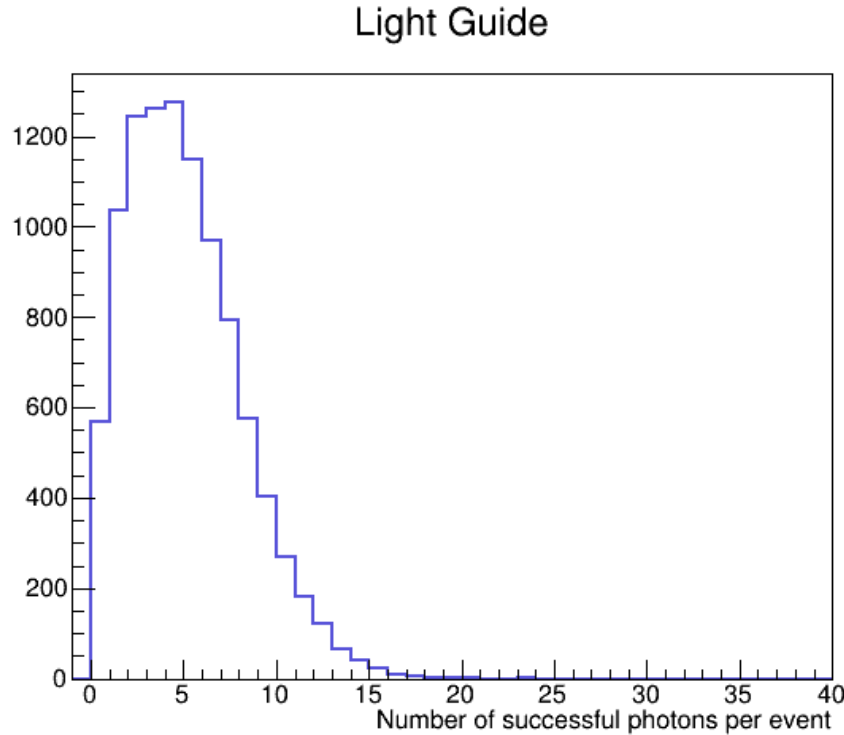


Figure 4.4: Photon output for the acrylic light guide design. Here, a photon is successful if it hits the sample of geometry.

4.2.2 Fiber Barrel

Standalone Monte Carlo Code

For the barrel design, a sample of the geometry was considered to be one 6 mm by 40 cm TPB doped fiber. The barrel had a mean of 12.13 successful photons per event and a mean of 11.98 after taking attenuation into account. As can be observed in Figure 4.5, the attenuation was not significant.

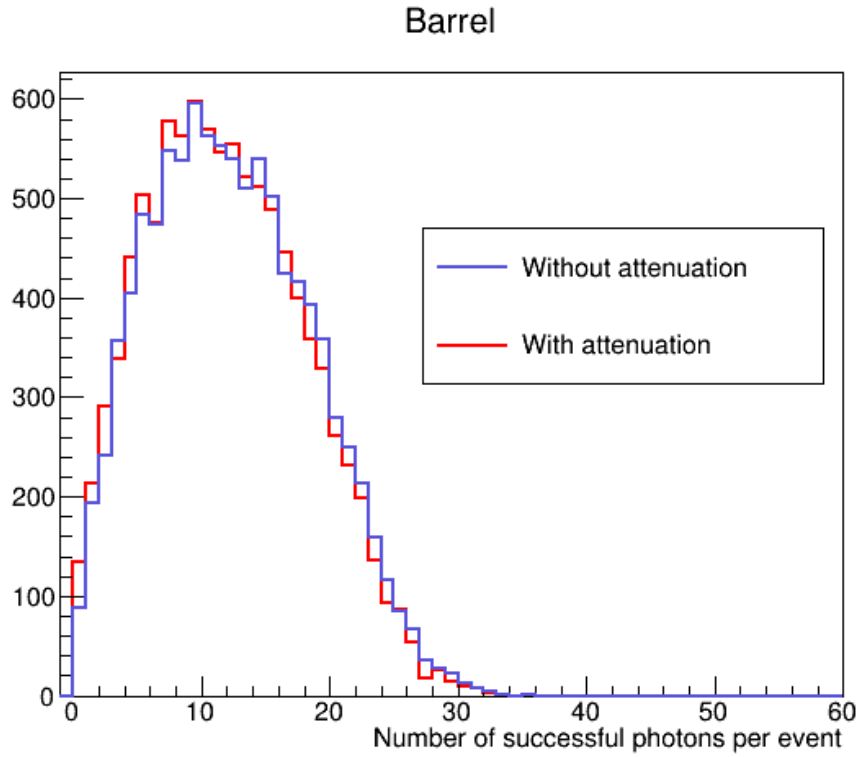


Figure 4.5: Photon output per event for the fiber barrel design.

A2Geant4: Individual Particles

Figure 4.6 shows the hits per SiPM when individual particles were thrown in the barrel design, assuming that 65 photons are emitted per MeV of energy deposited. It is not just the shape of the histograms that is important, but the number of entries for each particle type. The α particles get detected at the highest rate, which is encouraging since they are just a helium nucleus. Moreover, as the particle energy is increased, only the alpha has a higher mean — the rest stay relatively similar. A table summarizing the mean number of hits per SiPM for each particle type, particle energy, and scintillation yield is included in the Appendix in Table A.1.

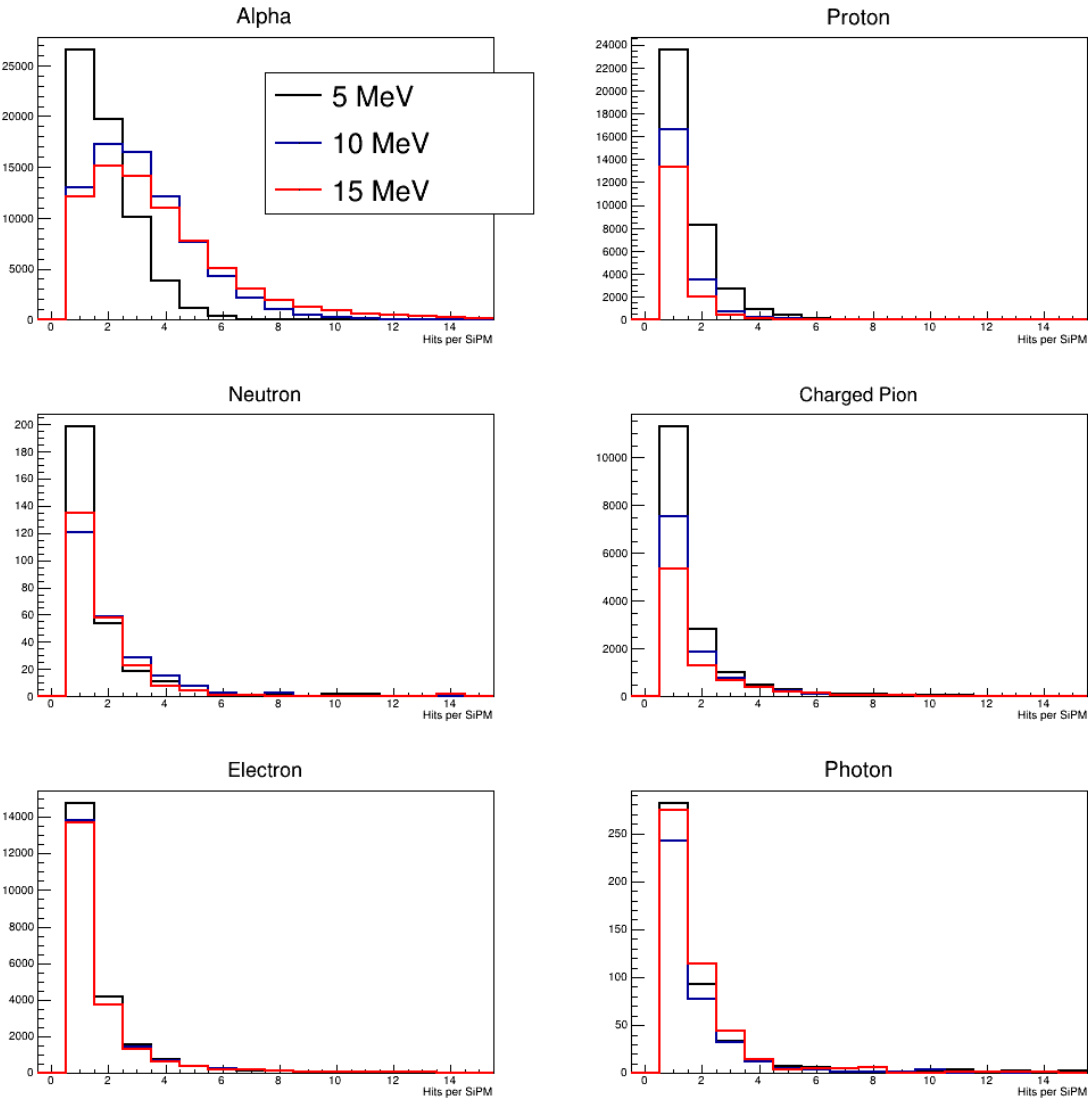


Figure 4.6: Hits per SiPM for various particle types at 5 (black), 10 (blue), and 15 (red) MeV. The scintillation yield was held constant at 65.

As seen in Section 3.1.1, the scintillation yield of pressurized gaseous helium is not precisely known, although it is estimated to be between 60 and 18000. Therefore, each process is repeated with three different scintillation yields: 65, 650, and 6500. The results for the α particle along with two important backgrounds, protons and photons, are shown in Figure 4.7.

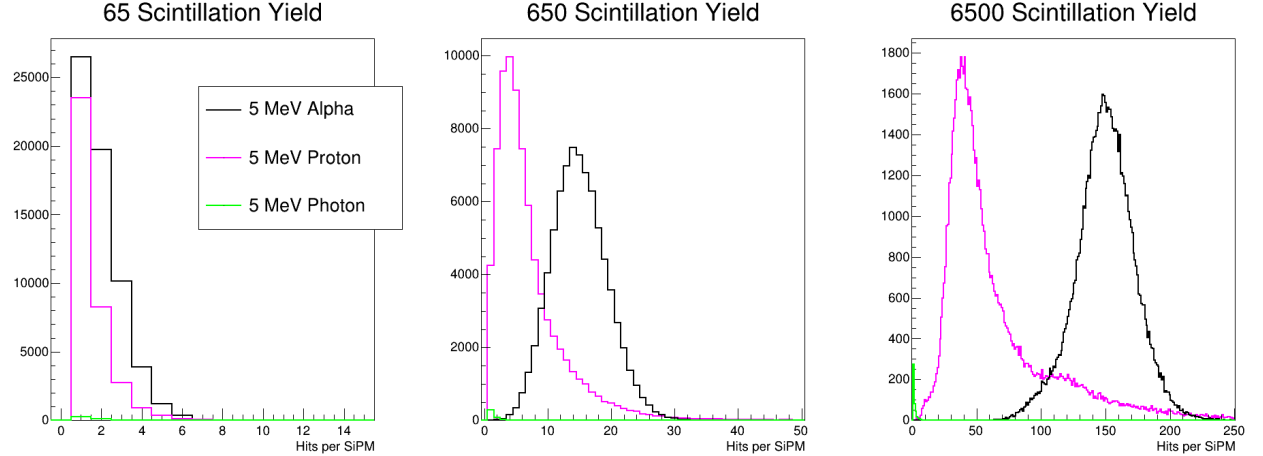


Figure 4.7: Hits per SiPM for α particles (black), protons (magenta), and photon (green). The scintillation yield was set to 65, 650, and 6500.

It can be observed that at the higher scintillation yields, the α particle signal increases more than the proton's. It should also be noted the the photon produces minimal scintillation light, even at the 6500 yield.

A2Geant4: EvGen File as Input

Simulations were also run with an EvGen file as input. The photon beam was set to 100, 150, and 200 MeV to cover a large range of energies, as seen in Figure 4.8. However, no data were simulated for neutral pion production at 100 MeV, seeing as it is below pion production energy threshold. To continue, a more energetic photon beam will result in more energetic recoil nuclei. This can be observed in the histograms, where the higher photon beam energies resulted in higher mean hits per SiPM.

As with the individual particle, the scintillation yield was varied for each process, as can be seen in Figure 4.9. A summary of the barrel results is shown in Table 4.2.

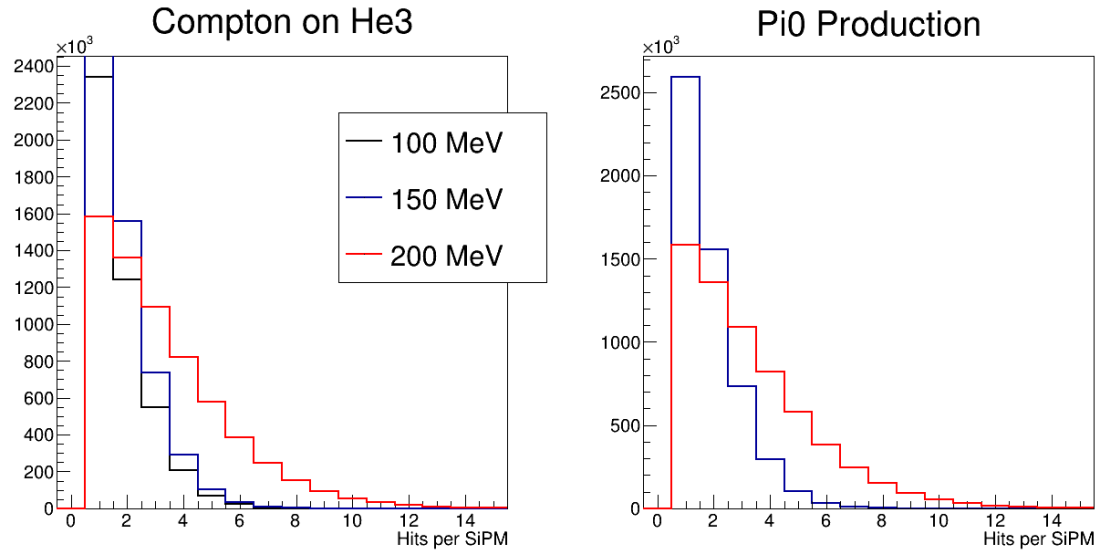


Figure 4.8: Hits per SiPM for Compton scattering off ${}^3\text{He}$ at 100, 150, and 200 MeV and neutral pion production at 150 and 200 Mev, with a scintillation yield of 65.

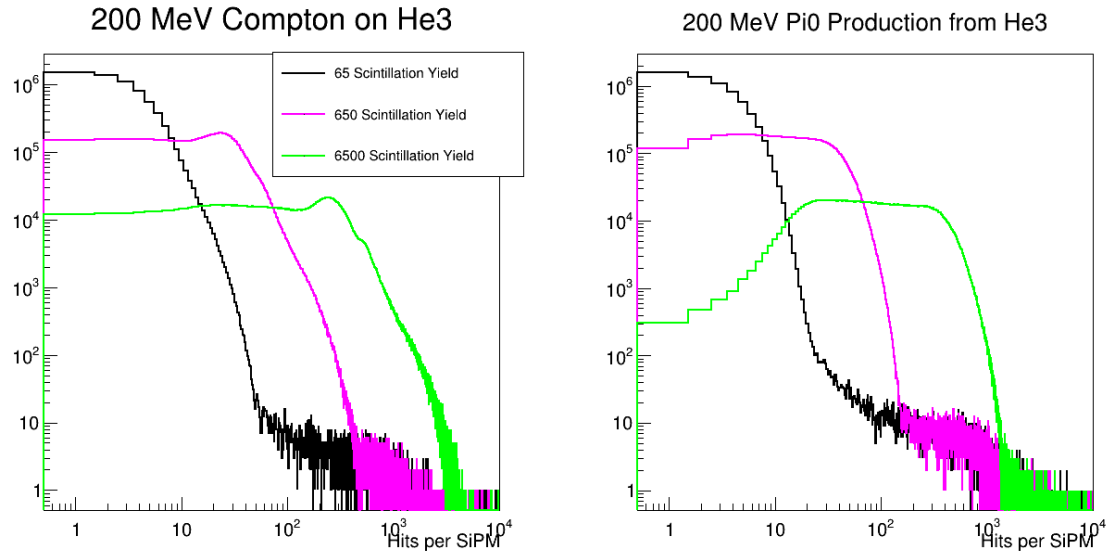


Figure 4.9: Hits per SiPM for Compton scattering and neutral pion production at 200 MeV. The simulation was run with a scintillation yield of 65 (black), 650 (magenta), and 6500 (green).

| Scintillation Yield | 65 | 650 | 6500 |
|------------------------|-------|--------|---------|
| Compton 100 MeV | 1.329 | 9.694 | 96.080 |
| Compton 150 MeV | 2.226 | 20.156 | 196.606 |
| Compton 200 MeV | 2.792 | 25.406 | 242.824 |
| Pi0 150 MeV | 1.494 | 11.992 | 119.074 |
| Pi0 200 MeV | 2.696 | 24.823 | 240.627 |

Table 4.2: Hits per SiPM results for Compton scattering on ${}^3\text{He}$ and neutral pion production in the barrel design at various photon beam energies and scintillation yields.

4.2.3 Fiber Helix

Standalone Monte Carlo Code

One sample of the helix design was considered to be one 0.5 mm TPB doped fiber wrapped 12 times to form a 6 mm spiral. The mean number of hits per SiPM per event was 8.42 and 6.79 with and without considering attenuation, respectively (see Figure 4.10). The signal loss was more appreciable with this design due to the long distances each photon must travel within the fiber before reaching a SiPM.

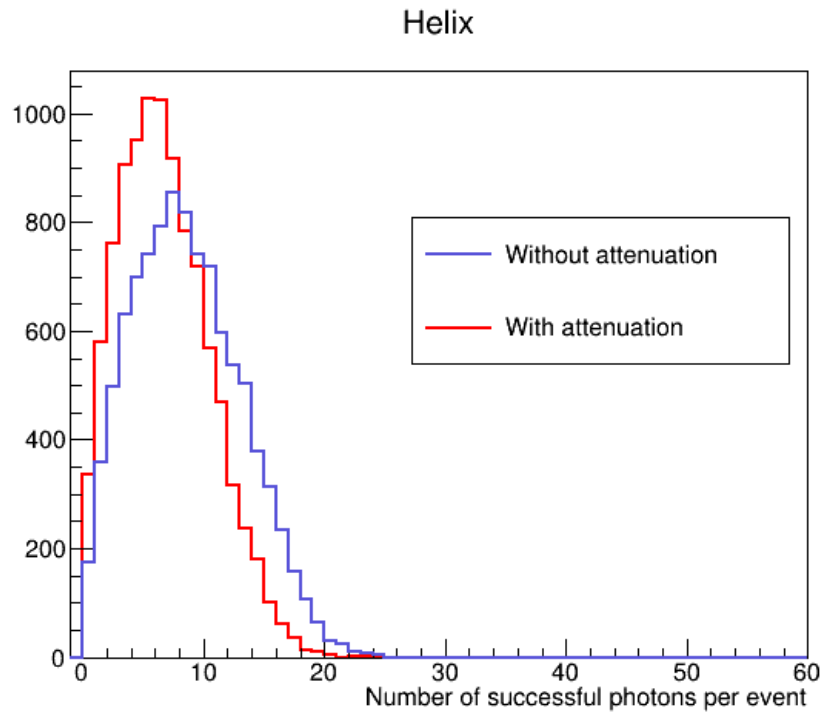


Figure 4.10: Photon output per event for the fiber helix design.

A2Geant4: Individual Particles

Figure 4.11 shows a sample of the helix results for an α particle being thrown at various energies and scintillation yields. An increase in particle energy or scintillation yield resulted in higher mean hits per SiPM, as expected.

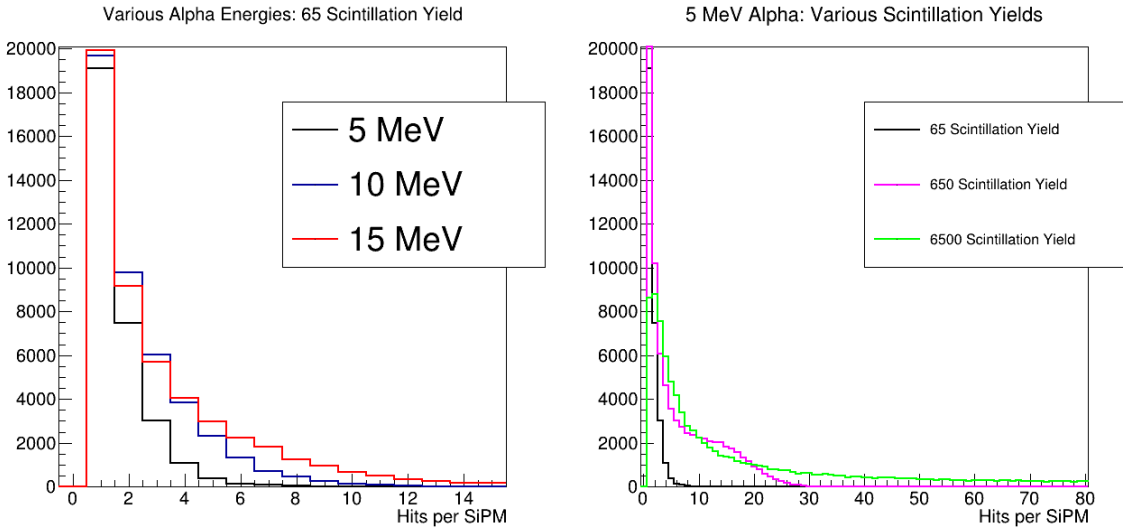


Figure 4.11: The leftmost histogram shows the hits per SiPM for α particles being thrown in the helix design with a set scintillation yield of 65. The histogram on the right shows the hits per SiPM for a 5 MeV α particle at the three scintillation yields.

A2Geant4: EvGen File as Input

The processes that were run with the barrel design were then repeated with the helix design. Similar results were obtained, although a better comparison is achieved by examining the mean of each histogram, shown for the helix in Table 4.3. Although the results appear to be relatively similar at the 65 scintillation yield, as this increases to the 650 and 6500 yields, it becomes obvious that the barrel design has far superior photon output.

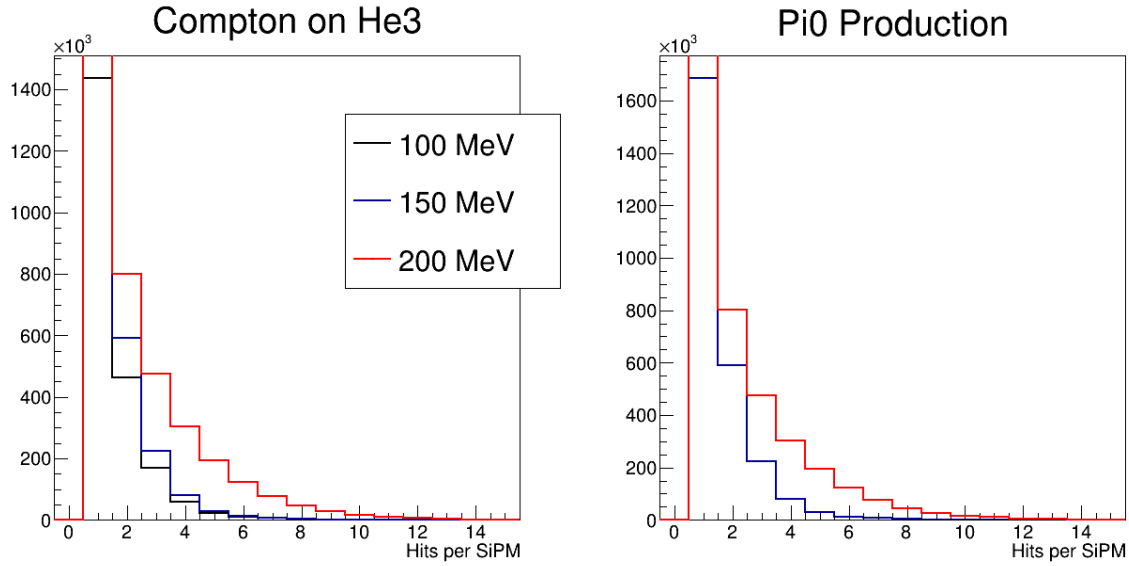


Figure 4.12: Hits per SiPM for Compton scattering off ${}^3\text{He}$ at 100, 150, and 200 MeV and neutral pion production at 150 and 200 MeV, with a scintillation yield of 65.

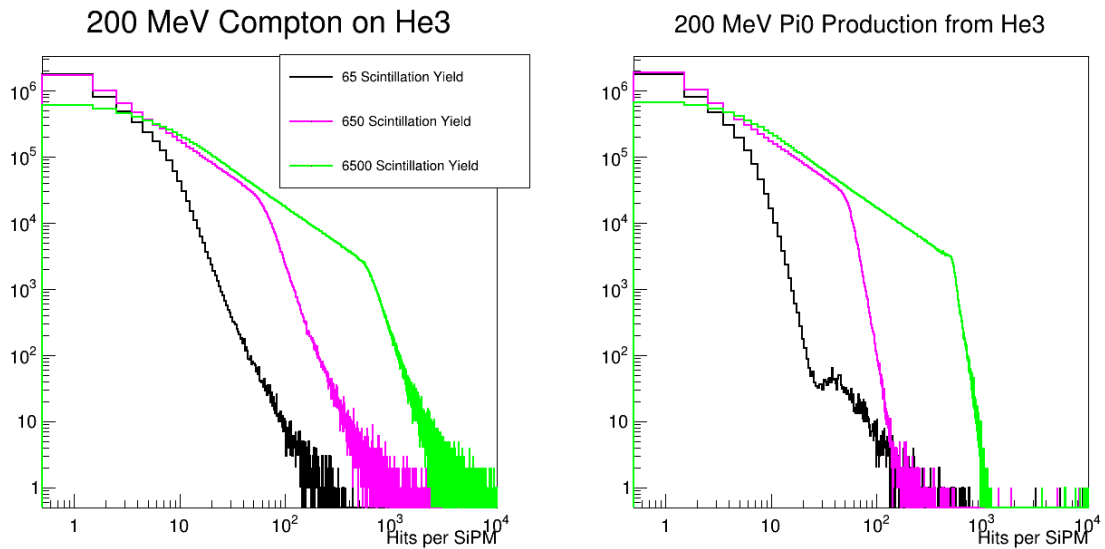


Figure 4.13: Hits per SiPM for Compton scattering and neutral pion production at 200 MeV. The simulation was run with a scintillation yield of 65 (black), 650 (magenta), and 6500 (green).

| Scintillation Yield | 65 | 650 | 6500 |
|------------------------|-------|-------|--------|
| Compton 100 MeV | 1.024 | 3.118 | 10.685 |
| Compton 150 MeV | 1.451 | 4.486 | 20.346 |
| Compton 200 MeV | 1.825 | 6.047 | 35.372 |
| Pi0 150 MeV | 1.103 | 3.540 | 12.521 |
| Pi0 200 MeV | 1.620 | 5.142 | 26.227 |

Table 4.3: Hits per SiPM results for Compton scattering on ${}^3\text{He}$ and neutral pion production in the helix design at various photon beam energies and scintillation yields.

Chapter 5

DISCUSSION AND OUTLOOK

As the AHeT has yet to be built, the results of this thesis, along with future analysis, will provide integral insight on the feasibility of helium scintillation light collection and the geometries that capture it.

Three new possible WLS geometries were analyzed. The acrylic light guide design was eliminated early on due to its low photon output in the preliminary simulation. More rigorous testing was completed on the barrel and helix designs using A2Geant4. This work showed that for both designs, the α particle had a higher photon output compared to backgrounds such as protons, neutrons, photons, etc. Although not evident at the lowest energy and scintillation yield, when these two parameters were increased, the α particle had peaks distinct from the rest of the backgrounds. This high photon output for α particles can also be observed in Tables A.2 and A.1, where the mean hits per SiPM for an α particle is higher than any other particle, in all cases. Simulations were also run with an EvGen file as input. In both designs, the photon output for Compton scattering was found to be quite similar to that of neutral pion production at 150 and 200 MeV. Fortunately, the primary region interest for the neutron scalar polarizabilities is below the pion production threshold energy. There is also interest in studying pion photoproduction itself, in which case the cross section for pion production is about 100 times larger than Compton events [Mar21].

In all processes that were run in the designs, increasing the energy and the scintillation yield gave better results. This was expected, since the number of photons emitted from a scattering event is dependent on the product of these two parameters.

It is important to note that the barrel design had significantly better light col-

lection than the helix design. As previously mentioned, the helix is currently approximated by rings in A2Geant4, and so this low output is without considering the significant attenuation that would take place with the actual geometry. Therefore, the results shown in this work are much higher than what the helix design would obtain in practice. This raises the question of permanently replacing the helix design with rings. The only downside with rings is that a small slice of phi is lost where the PCB and SiPMs would be inserted. However, that should be insignificant compared to the signal loss due to the attenuation from the spirals. More possible design modifications are explored in Appendix B, all of which will have to be considered further.

To conclude, there is more work that should be done to prepare for this experiment. The feasibility of the AHeT depends on the scintillation yield of helium along with the efficiency of the WLS geometry. Testing with TPB doped fibers should be conducted to get a better idea of the helium scintillation yield. Since these fibers must be ordered in bulk and are quite expensive, they could instead be borrowed from another research collaboration that already uses them. Although more simulations will have to be run in order to test each design thoroughly, this work provides a framework for further research to build upon.

References

- [Aad12] G. Aad et al., Phys. Rev. **716**, 1 (2012).
- [Ada18] D. L. Adams et al., Journal of Instrumentation **13**, P06022 (2018).
- [Ann13] J. Annand, D. Hornidge, A. Thomas, and E. J. Downie, Proposal for an Experiment: Compton Scattering on the He Isotopes with an Active Target, 2013.
- [Ann14] J. R. M. Annand, Compton Scattering on He using a High Pressure Gas Scintillator Active Target: An Investigation of a New Target Design, 2014.
- [Ann15] J. Annand, D. Hornidge, M. Morris, and B. Strandberg, AIP Conference Proceedings **1697**, 1 (2015).
- [Ben18] C. Benson, G. Gann, and V. Gehman, The European Physical Journal C **78** (2018).
- [CER21a] CERN, About root, 2021.
- [CER21b] CERN, Overview, 2021.
- [Cha12] R. Chandra et al., Journal of Instrumentation **7**, C03035 (2012).
- [Col15] C. Collicott, *Probing Proton Structure Through Single Polarization Observables of Compton Scattering and π^0 Photoproduction Within the $\Delta(1232)$ Region*, Ph. D. Thesis, Dalhousie University, 2015.
- [Deh11] M. Dehn et al., Eur. Phys. J. Special Topics **198**, 19–47 (2011).
- [Fey14] R. P. Feynman, *QED: The Strange Theory of Light and Matter*, Princeton University Press, Princeton, New Jersey, USA, 2014.
- [Geh11] V. Gehman et al., Nuclear Instruments and Methods in Physics Research A **654**, 116 (2011).
- [Gob21] S. Gobain, Optical Plastic Components, 2021.
- [Gri10] D. Griffiths, *Introduction to Elementary Particles*, WILEY-VCH, Portland, Oregon, USA, 2010.
- [Hag16] F. Hagelstein, R. Miskimen, and V. Pascalutsa, Prog. Part. Nucl. Phys **88**, 29 (2016).
- [Hal84] F. Halzen and A. Martin, *Quarks and Leptons*, John Wiley & Sons, USA, 1984.

- [Haw94] S. Hawking, *Black Holes and Baby Universes and Other Essays*, Bantam Books, New York, New York, USA, 1994.
- [Her76] H. Herminghaus et al., Nuclear Instruments and Methods **138**, 1 (1976).
- [Hoo17] K. M. Hood, *Proton Detection Efficiency with the Active Polarized Target*, Honours Thesis, Mount Allison University, 2017.
- [Hor15] D. Hornidge, Compton Scattering and Polarizabilities at MAMI, 2015.
- [Hor19] D. Hornidge, Compton Scattering and the Nucleon Polarizabilities, 2019.
- [Hor20] D. Hornidge, Private Communication, 2020.
- [ICM21] T. ICM, How to choose your x-ray source, 2021.
- [Ito13] T. M. Ito and G. M. Seidel, Phys. Rev. C **88** (2013).
- [Jeb13] R. A. Jebali, *Measurement of the $\gamma + {}^4\text{He}$ Total Photoabsorption Cross-Section using a Gas-Scintillator Active Target*, Ph. D. Thesis, University of Glasgow, 2013.
- [Kai08] K. H. Kaiser and et al., Nucl. Instrum. Methods Phys. Res. Sect. A **593** (2008).
- [Kie13] C. Kiefer, International Scholarly Research Notices **2013**, 17 (2013).
- [KPH09] KPH, The Mainz Microtron, 2009, Institut für Kernphysik, Johannes Gutenberg Universität.
- [KPH19] KPH, What does the A2 Collaboration do? , 2019, Institut für Kernphysik, Johannes Gutenberg Universität.
- [Kur21] Kuraray, Wavelength Shifting Fibers, 2021, Data Sheet.
- [Led93] L. Lederman, *The God Particle: If the Universe is the Answer, what is the Question?*, Houghton Mifflin Company, New York, 1993.
- [MAM21] MAMI, A2 Detector System, 2021, Institut für Kernphysik, Johannes Gutenberg Universität.
- [Mar21] P. Martel, Private Communication, 2021.
- [McG08] J. McGeorge et al., The European Physical Journal A **37**, 129 (2008).
- [Mor16] M. Morris, *Neutron Scalar Polarizabilities: Background Simulations for Experimental Extraction via Compton Scattering from ${}^3\text{He}$* , Honours Thesis, Mount Allison University, 2016.
- [Neg21] M. D. Negra, P. Jenni, and T. S. Virdee, Phys. Rev. **338**, 1560 (2021).

- [Pat16] C. Patrignani et al., Chinese Physics C **40** (2016).
- [Per17] M. S. Perry, *Investigation of Wavelength Shifting Materials in an Active Helium Target and Detection Efficiencies*, Honours Thesis, Mount Allison University, 2017.
- [Sch21] H. C. Schoultz-Coulon, Scintillator Detectors, 2021, Presentation.
- [Sen17] SensL, J-Series High PDE and Timing Resolution, TSV Package, 2017, Data Sheet.
- [Shu09] D. Shukla, A. Nogga, and D. R. Phillips, Nuclear Physics A **819** (2009).
- [Tho16] A. Thomas, EPJ Web of Conferences **130**, 3 (2016).
- [Tip08] P. Tipler and R. Llewellyn, *Modern Physics, fifth Edition*, W. H. Freeman Company, 41 Madison Avenue, New York, NY, USA, 2008.
- [Wen17] M. Wentland, *Neutron Scalar Polarizabilities*, Honours Thesis, Mount Allison University, 2017.
- [Wik20] Wikipedia, Standard Model of Elementary Particles, 2020.
- [Wik21] Wikiwand, The MAMI Accelerator, 2021.

Appendix A

Tabulated Results

A.1 Calculation Method

These tables are not the raw mean from the histograms, but rather the mean after making some cuts. For the barrel, an event is only counted when 9 or more SiPMs register a signal. For the helix, when 5 or more register a signal. This allowed for backgrounds to be ignored, since helium scattering events shower over several fibers.

A.2 Throwing Particles

| Scintillation Yield | | 65 | 650 | 6500 |
|---------------------|----------|-------|--------|---------|
| 5 MeV Particles | Alpha | 1.847 | 14.771 | 147.970 |
| | Proton | 1.113 | 6.003 | 56.711 |
| | Neutron | 0.012 | 0.042 | 0.303 |
| | Pion | 0.752 | 1.880 | 14.502 |
| | Electron | 1.100 | 1.140 | 2.001 |
| | Photon | 0.019 | 0.023 | 0.024 |
| | Alpha | 2.916 | 27.879 | 268.675 |
| | Proton | 1.005 | 3.220 | 29.225 |
| | Neutron | 0.007 | 0.031 | 0.163 |
| | Pion | 0.430 | 1.289 | 6.498 |
| 10 MeV Particles | Electron | 1.099 | 1.143 | 1.983 |
| | Photon | 0.018 | 0.025 | 0.044 |
| | Alpha | 3.220 | 30.592 | 289.863 |
| | Proton | 0.903 | 2.430 | 21.072 |
| | Neutron | 0.009 | 0.022 | 0.231 |
| | Pion | 0.276 | 1.185 | 4.731 |
| 15 MeV Particles | Electron | 1.082 | 1.118 | 1.996 |
| | Photon | 0.021 | 0.027 | 0.024 |

Table A.1: Mean hits per SiPM results for different particles thrown in the barrel design at 5, 10, and 15 MeV and for scintillation yields set at 65, 650 and 6500 photons emitted per MeV of energy deposited in the active volume.

| Scintillation Yield | | 65 | 650 | 6500 |
|---------------------|----------|-------|-------|--------|
| 5 MeV Particles | Alpha | 1.114 | 4.029 | 14.500 |
| | Proton | 1.042 | 2.920 | 10.085 |
| | Neutron | 0.010 | 0.033 | 0.100 |
| | Pion | 0.617 | 1.424 | 4.811 |
| | Electron | 1.031 | 1.094 | 1.460 |
| | Photon | 0.003 | 0.006 | 0.023 |
| | Alpha | 1.839 | 5.462 | 27.626 |
| | Proton | 0.978 | 2.255 | 7.825 |
| | Neutron | 0.006 | 0.018 | 0.018 |
| | Pion | 0.259 | 1.077 | 3.212 |
| 10 MeV Particles | Electron | 1.002 | 1.032 | 1.444 |
| | Photon | 0.001 | 0.006 | 0.010 |
| | Alpha | 2.089 | 6.406 | 40.388 |
| | Proton | 0.883 | 1.804 | 6.354 |
| | Neutron | 0.006 | 0.010 | 0.085 |
| | Pion | 0.135 | 1.026 | 2.660 |
| 15 MeV Particles | Electron | 0.935 | 1.080 | 1.353 |
| | Photon | 0.016 | 0.003 | 0.013 |

Table A.2: Mean hits per SiPM results for different particles thrown in the helix design at 5, 10, and 15 MeV and for scintillation yields set at 65, 650 and 6500 photons emitted per MeV of energy deposited in the active volume.

A.3 Using EvGen Files as Input

The following two tables outline the results for different processes being run in the barrel and helix designs. EvGen files for each of the processes were used as input. The median was calculated following the same steps as explained in Section A.1.

| Scintillation Yield | 65 | 650 | 6500 |
|----------------------------|-----------|------------|-------------|
| Compton 100 MeV | 1.329 | 9.694 | 96.080 |
| Compton 150 MeV | 2.226 | 20.156 | 196.606 |
| Compton 200 MeV | 2.792 | 25.406 | 242.824 |
| Pi0 150 MeV | 1.494 | 11.992 | 119.074 |
| Pi0 200 MeV | 2.696 | 24.823 | 240.627 |

Table A.3: Hits per SiPM results for Compton scattering on ${}^3\text{He}$ and neutral pion production in the barrel design at various photon beam energies and scintillation yields.

| Scintillation Yield | 65 | 650 | 6500 |
|----------------------------|-----------|------------|-------------|
| Compton 100 MeV | 1.024 | 3.118 | 10.685 |
| Compton 150 MeV | 1.451 | 4.486 | 20.346 |
| Compton 200 MeV | 1.825 | 6.047 | 35.372 |
| Pi0 150 MeV | 1.103 | 3.540 | 12.521 |
| Pi0 200 MeV | 1.620 | 5.142 | 26.227 |

Table A.4: Hits per SiPM results for Compton scattering on ${}^3\text{He}$ and neutral pion production in the helix design at various photon beam energies and scintillation yields.

Appendix B

Possible Design Modifications

If the light collection is low (as is the case with the helix/rings design), many fibers may be coupled to each SiPM. For the barrel design, the 6 mm fibers may be replaced by 3 mm fibers, in which case 4 fibers may be coupled to each SiPM. This way, the 4 fibers form a 6 mm ‘plate’, covering more area. Similar modifications can be made to the helix design to increase the effective area covered by each SiPM. The helix/ring design is limited to the 0.5 mm fibers due to cracking. However, the ring size could be increased to a maximum of 72 mm. This would have a large impact on light collection.

| Fiber size | Fibers per SiPM | Effective ‘plate’ |
|------------|-----------------|-------------------|
| 6 mm | 1 | 6 mm |
| 3 mm | 4 | 12 mm |
| 2 mm | 9 | 18 mm |
| 1 mm | 36 | 36 mm |
| 0.5 mm | 144 | 72 mm |

Table B.1: Possible fiber to SiPM couplings for the barrel and ring designs.